Weather and Climate Extremes 37 (2022) 100472

Contents lists available at ScienceDirect

Weather and Climate Extremes

journal homepage: www.elsevier.com/locate/wace

An extraordinary dry season precipitation event in the subtropical Andes: Drivers, impacts and predictability

Raúl Valenzuela [a,c], René Garreaud [b,c,*], Iván Vergara [d], Diego Campos [e], Maximiliano Viale [f], Roberto Rondanelli [b,c]

[a] Universidad de O'Higgins, Rancagua, Chile
[b] Universidad de Chile, Santiago, Chile
[c] Centro de Ciencia del Clima y la Resiliencia (CR2), Santiago, Chile
[d] Instituto Andino Patagónico de Tecnologías Biológicas y Geoambientales (IPATEC), Bariloche, Argentina
[e] Dirección Meteorológica de Chile, Santiago, Chile
[f] Instituto Argentino de Nivología, Glaciología y Ciencias Ambientales (IANIGLA), Mendoza, Argentina

ARTICLE INFO

Keywords:
Extreme precipitation
Subtropical Andes
Atmospheric rivers
Landsides

ABSTRACT

A major storm impacted the subtropical Andes during 28–31 January 2021 producing 4-days accumulated precipitation up to 100 mm over central-south Chile. These are high accumulations even for winter events but the storm occurred in the middle of the summer when precipitation is virtually absent, conferring it an extraordinary character. Similar storms have occurred only 2–3 times in the past century. The January 2021 event included periods of high rainfall intensity, hail and lighting, causing dozens of landslides and flash floods with the concomitant social impacts and economical losses. Here we examine the meteorological drivers of this storm at multiples scales, its climatological context, the associated surface impacts, and some aspects of its predictability.

About a week before the storm development over central Chile, a large-scale perturbation in the central South Pacific set the stage for the formation of a zonal jet aloft and zonal atmospheric river (ZAR) that extended eastward until reaching the west coast of South America. The ZAR landfalled at 39°S and its subsequent northward displacement resulted in copious orographic precipitation over the Andes and adjacent lowlands, concomitant with a relatively warm environment during the first phase of the storm (28–29 January). During the second phase (30–31 January) the ZAR decayed rapidly but left behind significant amount of water vapor and the formation of a cut-off low (COL) in its poleward flank. The COL facilitated both advection of cyclonic vorticity and cold air at mid-levels, setting the environment for deep convection, intense rain showers, significant lightning activity, and hail.

An assessment of the quantitative precipitation forecast (QPF) from the operational Global Forecast System (GFS) indicates that the model captured well the 96-h precipitation accumulation (28–31 January) in terms of timing and spatial extent. However, specific zones with the largest accumulations varied as a function of lead time. The more stable precipitation during the ZAR phase was better predicted than the convective precipitation during the COL phase. Proper dissemination of these forecast and recently established infrastructure contributed to ease the impact of this extraordinary event on the general population.

1. Introduction

The frequency and intensity of extreme precipitation events are increasing in many regions worldwide, seemingly in connection with global warming mediated by the higher water vapor content of the troposphere or changes in atmospheric circulation (e.g., Meehl et al., 2000; Allen and Ingram, 2002; Donat et al., 2016; Pendergrass et al., 2017; Zhang et al., 2021). This enhanced meteorological threat is coupled with an increase in population exposure -and vulnerability in some cases- resulting in dramatic social, economic and environmental impacts (e.g., Dominguez and Coauthors, 2018). Nonetheless, the nature of extreme events is highly dependent on the region and season in which they occur, calling for in-depth studies of especially damaging or unusual cases to assess their dynamics, exceptionality and the possible

* Corresponding author. Blanco Encalada , 2002, Santiago, Chile.
E-mail address: rgarreau@uchile.cl (R. Garreaud).

https://doi.org/10.1016/j.wace.2022.100472
Received 4 February 2022; Received in revised form 6 May 2022; Accepted 7 June 2022
Available online 14 June 2022

connection with climate change. These studies may also contribute to evaluate the predictability of extreme events by the current generation of atmospheric models as well as to project their behavior in a future climate.

One of such extreme storms occurred in central-south Chile between 28 and 31 January 2021. The storm was exceptional because of the large amount of precipitation it delivered and its occurrence in the middle of the summer, the absolute dry season in this subtropical region. Precipitation was most intense over the western side of the subtropical Andes but also reached the eastern side of the mountains (Argentina), and it took place in a warmer environment relative to the more common winter storms, augmenting the hydrological response of the rivers rooted in the Andes. Consistently, the storm caused dozens of landslides and flash floods in the most heavily populated part of the country, resulting in numerous and substantial impacts in the population, infrastructure and agriculture (Garreaud et al., 2021).

Central Chile, the narrow strip of land between the Pacific Ocean and the subtropical Andes (32–36°S, Fig. 1a), hosts more than 10 million inhabitants along with intense agriculture, mining and services. It encompasses four administrative regions (Valparaiso, Metropolitan, O'Higgins and Maule) and many important cities (including Santiago, the Chilean capital) along the major north-south valley next to the Andes foothills. This region features a semi-arid (100–1000 mm yr^{-1}), Mediterranean-like climate in which most of precipitation (>70%) is accounted for a handful of storms during winter months (Aceituno et al., 2021). From May to September the semi-permanent anticyclone over the subtropical southeast Pacific moves northward allowing the arrival of frontal systems to the continent, many of them accompanied by Atmospheric Rivers (about 1–9 ARs per winter, Viale et al., 2018). AR transports vast amounts of moisture in a narrow band that, when forced to ascent over the western slopes of the Andes (reaching 3–5 km of altitude in these latitudes), generate substantial precipitation. Of particular interest is the occurrence of zonally elongated atmospheric rivers (hereafter referred as ZAR) in connection with warm and heavily precipitating storms in central Chile during winter (Garreaud, 2013; Valenzuela and Garreaud, 2019). Similar mechanisms operate in other mountainous regions at subtropical and mid-latitudes, most documented along the west coast of North America (e.g., Neiman et al., 2011).

By the contrary, the southward migration of the subtropical anticyclone and storm track during austral summer hampers the arrival of frontal systems and ARs to central Chile. Consistently, rain is nearly absent over the coast and interior valleys from December to February, with long-term mean accumulations below 10 mm (Fig. 1b), less than 5% of the annual mean. Higher up over the western side of the subtropical Andes, the summertime accumulation increases to 20–40 mm, still less than 10% of the annual total. Summer precipitation is mostly caused by isolated, convective storms atop of the Andes often fed by moisture sourced over the interior of the continent and the Atlantic Ocean (e.g., Aceituno et al., 2021), which can trigger localized debris flows up in the Andes (Vergara et al., 2020). Thus, the late January 2021

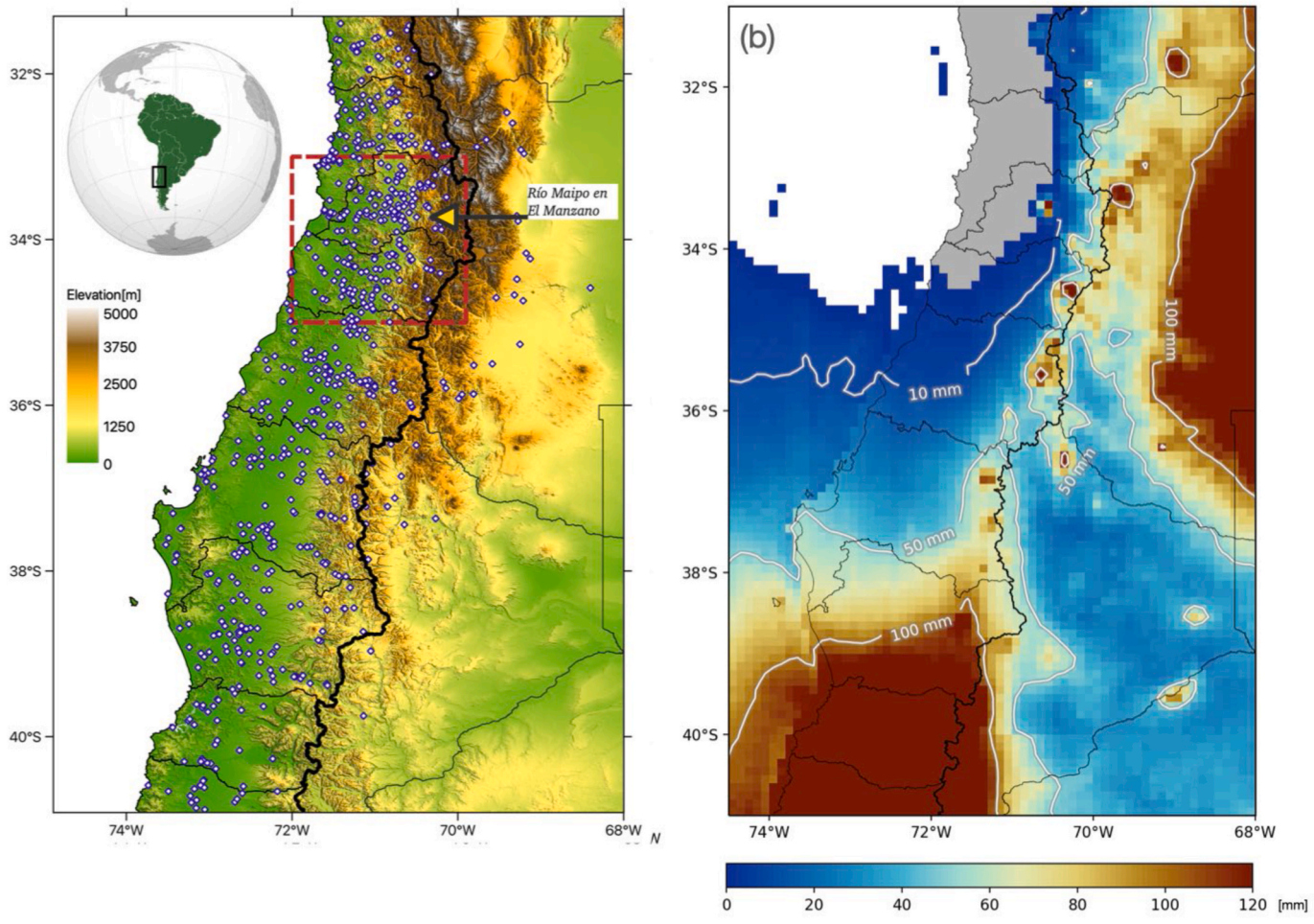

Fig. 1. Study domain showing: (a) locations of the rain gauges (circles) and terrain elevation (color coded) and (b) December through February (DJF) mean precipitation between 2000 and 2020 from IMERG Final Run. Red dashed line in (a) indicates latitude-longitude box 33°–35°S and 69.9°W–72°W used for ERA5 analysis and arrow annotation shows the location of hydro-sedimentary variable measurements. (For interpretation of the references to color in this figure legend, the reader is referred to the Web version of this article.)

storm brought substantial precipitation at coastal, interior and Andean sectors of central Chile in the middle of the dry season and was perceived as extraordinary by the general population and the media. Furthermore, this summer event featured ingredients that are typical of winter storms (Falvey and Garreaud, 2007).

This study provides a multiscale analysis of the processes that lead to the extreme precipitation event of 28-31 January 2021 over the subtropical Andes and the adjacent lowlands of central Chile and parts of western Argentina. The multiple datasets used for this analysis are presented in section 2. Sections 3.1-3.4 present the meteorological analyses from the local to synoptic to hemispheric scales. The uniqueness of the event is explored in section 3.5 using long-term time series and their main impacts are described in section 3.6. The performance of the publicly available Global Forecast System to predict the event is analyzed in section 3.7. A discussion and conclusions are presented in section 4.

2. Data and methods

Hourly records from a total of 553 rain gauge stations covering continental Chile between 30°S and 45°S were obtained from *Dirección Meteorológica de Chile (DMC)*, *Dirección General de Aguas (DGA)*, *Agromet, Centro de Estudios Avanzados en Zonas Áridas (CEAZA),* and *Redmeteo* through the Center for Climate and Resilience Research (CR2)'s Vismet platform (https://vismet.cr2.cl). In addition, 37 rain gauge stations from Argentina's *Departamento General de Irrigación-Mendoza*, *Servicio Meteorológico Nacional*, *Base Hídrica Nacional*, *Autoridad Interjurisdiccional de las Cuencas-Neuquen* were included in the study to cover the eastern side of the Andes (Fig. 1a).

Satellite precipitation estimates from the Integrated Multi-satellite Retrievals for GPM (IMERG) with gauge calibration half-hourly 0.1° × 0.1° Final Run product (GPM_3IMERGHH v06, Huffman et al., 2015) were employed to obtain a continuous overview of the accumulated precipitation during the 28–31 January 2021 storm and describe general precipitation patterns, especially over the Andes and offshore where precipitation gauges are absent. Furthermore, IMERG monthly 0.1° × 0.1° Final Run product (GPM_3IMERGM v06, Huffman et al., 2015) was employed to describe the dry season climatology (December through February) between 2000 and 2021. Both products were obtained using NASA's Giovanni platform (https://giovanni.gsfc.nasa.gov/giovanni/).

To understand the hydrometeorological impacts of the storm, an inventory of observed landslides was built, and hydro-sedimentary variables were analyzed. For landslides, the date and location of each event was collected from newspapers, technical reports of emergency authorities, and Twitter accounts of government entities and local inhabitants. For the hydro-sedimentary variables, hourly streamflow and turbidity of the Maipo River, which drains a basin of about 5000 km^2 and is located in one of the most impacted areas (Fig. 1a), were obtained from DGA and the *Aguas Andinas* company.

Continuous 5-min resolution time series of precipitable water (PW) from GPS receivers (GPS-PW) were employed to analyze the behavior of water vapor as the storm progressed. GPS data for Santo Domingo station (33.65°S, 71.61°W) was obtained from the Nevada Geodetic Laboratory (NGL) public archive (http://geodesy.unr.edu/PlugNPlayPortal.php), which provides processed Zenith Total Delay (ZTD) and PW values. GPS-PW data was bias corrected using precipitable water from radiometer observations from the closest Aeronet station in Santiago (Beauchef, 33.457°S, 70.662°W, https://aeronet.gsfc.nasa.gov/).

Lightning activity was obtained from the Geostationary Lightning Mapper (GLM) aboard the GOES-16 satellite (Rudlosky et al., 2019, Nesbitt and Coauthors, 2021). The instrument continuously detects intra and cloud-to-cloud lightning with an efficiency greater than 70% and false alarm rate less than 5%. Measurements are collected by a Charge-Coupled Device imager sensitive to light in a ~1-nm band centered at 777.4 nm (near infrared) with 2-ms temporal resolution and ~8 km spatial resolution. Flash locations during the storm were retrieved from the web platform https://georayos.citedef.gob.ar/.

The large-scale circulation during the storm was characterized using the ERA5 reanalysis of the European Centre for Medium-Range Weather Forecasts (Hersbach and Coauthors, 2020) with hourly resolution on a 0.25° × 0.25° lat-lon grid and 137 vertical levels. In addition to the three-dimensional pressure level variables (temperature, geopotential, and wind) we also employed two-dimensional fields including large-scale and convective precipitation rates, convective available potential energy (CAPE), integrated water vapor transport (IVT), and precipitable water (PW). Data were obtained through the Copernicus Climate Data Store archive (https://cds.climate.copernicus.eu/).

Operational quantitative precipitation forecasts (QPF) at 0.25° × 0.25° lat-lon resolution with 6-h accumulations produced by the Global Forecast System (GFS, Environmental Modeling Center, 2003) were used to explore how far in advance such an extraordinary event could be foreseen. The data was obtained from NCAR's Research Data Archive (RDA) using the THREDDS data server and Python's Siphon library. Surface precipitation gauge observations were spatially aggregated by computing the average value of all gauges included on the same 0.25° × 0.25° grid boxes as GFS (Fig. 2a) and grid-to-grid verification metrics were derived using the Model Evaluation Tools software,[1] developed and maintained by the Developmental Testbed Center (DTC, Brown and Coauthors, 2021). Twenty members of the NCEP Global Ensemble Forecast System (GEFS V12; Guan et al., 2020) were obtained from the Amazon Web Service (available at https://noaa-gefs-retrospective.s3.amazonaws.com/index.html). The GEFS ensembles are on the same 0.25° × 0.25° grid boxes as GFS, initialized every 6-h and available up to 10 days ahead of initial time.

3. Results

3.1. Surface precipitation features

The accumulated precipitation from 28 to January 31, 2021 is shown in Fig. 2a and b on the basis of gridded 0.25° × 0.25° *in-situ* observations and IMERG satellite estimates (see section 2). Both fields agree qualitatively, and their point-to-point correlation reaches 0.73 (significant at $p = 0.01$, see Sup. Fig. 1). The area with precipitation in Chile extended from 40°S (Los Ríos region) up until 32°S (northern limit of the Valparaiso region) where it sharply ended. There is a non-systematic meridional variation but a 2- to 3-fold increase from the coast to the western slopes of the Andes where storm accumulations exceeded 60 mm. Unfortunately, the coverage of precipitation gauges over terrain higher than 1500 m above sea level (ASL) is very low, but at least 3 gauges at about 3500 m ASL reported snow water equivalent values between 50 mm and 100 mm. Furthermore, observations and IMERG estimates suggest three sectors of precipitation maxima (>90 mm) over the Andean foothills at 33–35°S, ~37°S and ~39°S. The area with precipitation also encompassed the eastern side of the Andes and the adjacent lowlands several hundred of km east of the continental divide, with large rain and snow values (up to 50 mm) downstream of the precipitation maxima found in the Chilean side. The large magnitude of the end of January 2021 storm can be seen by comparing Fig. 2a with the precipitation climatology for summer months over the subtropical Andes presented in Fig. 1b. A fourth precipitation maxima, only visible from IMERG data, was located offshore at about 34°S.

The storm accumulation was caused by several periods of intense precipitation that are illustrated in Fig. 3a by a time-latitude cross section constructed with the hourly intensity data recorded in Chilean stations. There is a first, massive pulse that originated at about 39°S on the evening of 28 January and progressed steadily (at about 20 km h^{-1}) to reach 32.5°S by the dawn of 30 January. There is a similar northward moving pulse that initiated about one day later and reached Santiago

[1] https://dtcenter.org/community-code/model-evaluation-tools-met.

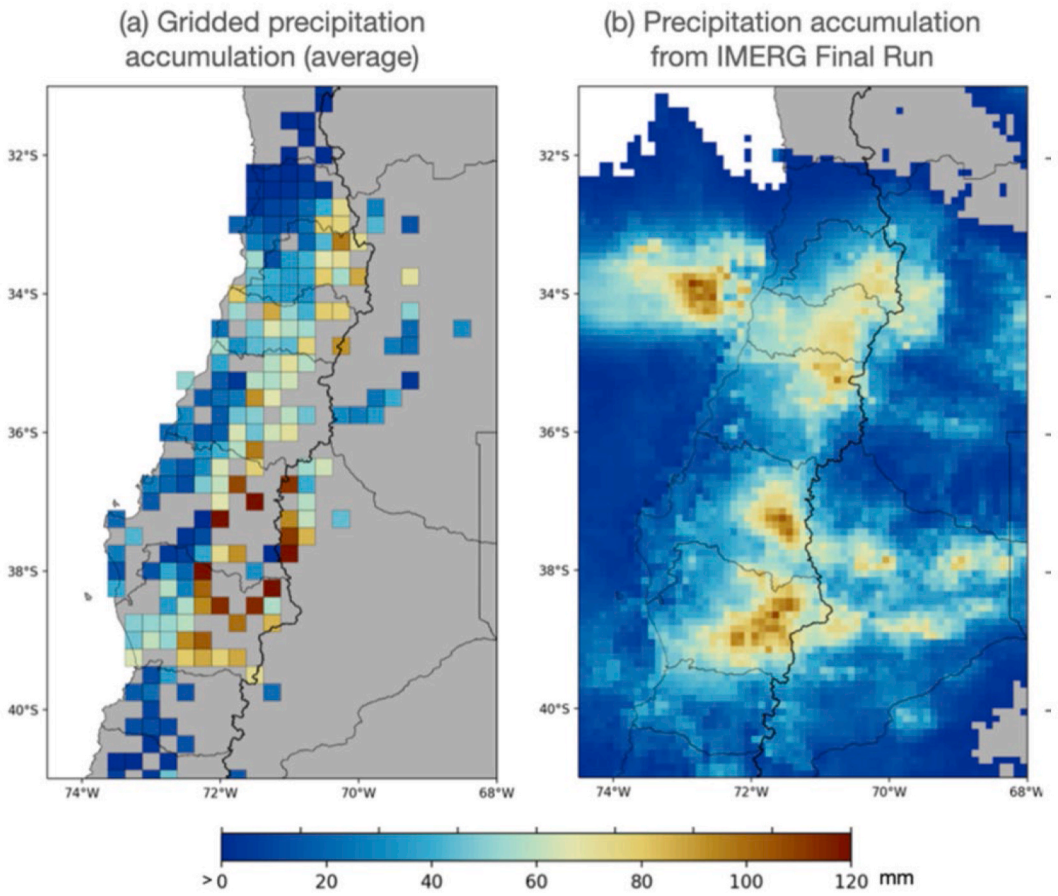

Fig. 2. Observed storm precipitation (accumulation from 28 to 31 January 2021) from (a) gridded 0.25° × 0.25° *in-situ* observations, (b) 0.1° × 0.1° IMERG Final Run product.

(~33.5°S) in the evening of 30 January. Later on, intense precipitation occurred rather simultaneously along the Andean foothills during the night of 30–31 January and the evening of 31 January. In general, moderate rain rates (<4 mm h^{-1}) dominated the first pulse while the highest rain rates (>6 mm h^{-1}) were observed during the second, third and fourth precipitation pulses.

3.2. Local meteorological conditions

The temporal evolution of some relevant ERA5 variables averaged over central Chile (the continental sector between 33 and 35°S; red dashed line in Fig. 1) are depicted in Fig. 4. Time series of hourly precipitation intensity, large-scale precipitation component, and the maximum precipitation rate (Fig. 4a) show that precipitation begins in central Chile during the afternoon of 29 January and reach a peak (>3 mm h^{-1}) through 29 January at night and the dawn of 30 January. Within this period, precipitation was largely dominated by the large-scale component. From the afternoon of 30 January to the end of 31 January the area-mean precipitation rate decreased to about 1 mm h^{-1} and, in sharp contrast with the first period, was dominated by the convective component. The rapid onset in area-mean precipitation and its more gradual demise tends to follow the evolution of precipitable water (PW) and lower tropospheric water vapor mixing ratio (r_{700}) over central Chile (Fig. 4c). The maximum PW~25 mm occurred at 00 UTC 30 January and is more than twice the pre- and post-storm values. These ERA5 values agrees well with estimates based on GPS data along the coast at Santo Domingo (33.65°S, Sup. Fig. 2). As we show later, the increase in water vapor over central Chile was due to a strong horizontal moisture transport from the Pacific (IVTx in Fig. 4b) in connection with the arrival of a zonal atmospheric river (see next section).

Despite the decrease in area-mean precipitation after midday of 30 January, ERA5 and *in-situ* precipitation data indicate that some of the highest localized rain-rates occurred in this last period of the storm. The emergence of lightning (Sup. Fig. 3) and the presence of hail on the ground (Romero et al., 2022) further supports the notion of strong convection developing in the evening of 30 and 31 January. To further quantify this aspect, Fig. 4d shows ERA5 hourly series of surface based Convective Available Potential Energy (CAPE) averaged over central Chile. CAPE was near zero during the first part of the storm (until the morning of 30 January) but then reached more than 500 J kg^{-1} in the evening of the next three days. Such large values of CAPE (for the context of central Chile) were favored by the return of daytime surface heating, a gradual cooling of the middle troposphere and a moist lower troposphere. The transition between a stable precipitation phase and convective pulses is a key element of the storm that we interpret later in the context of the synoptic evolution.

3.3. Precedent large-scale conditions

Between 10 and 5 days before the summer storm in central Chile, the extratropical circulation was largely zonal across the South Atlantic and Indian oceans but meridionally perturbed in the South Pacific showing a wavenumber 3 structure (Fig. 5a). In this sector there was a deep ridge centered at 150°W reaching to the Antarctic periphery accompanied by mid-latitude troughs over New Zealand and the eastern South Pacific. The trough-ridge-trough conformed an inverted omega pattern (e.g., de Lima Nascimento and Ambrizzi, 2002; Mendes et al., 2008), evident in the lower, middle and upper-troposphere, and ducting energy from the subtropical Southwest Pacific toward the east side of the basin. Such Rossby wave trains are common in the South Pacific and they can be

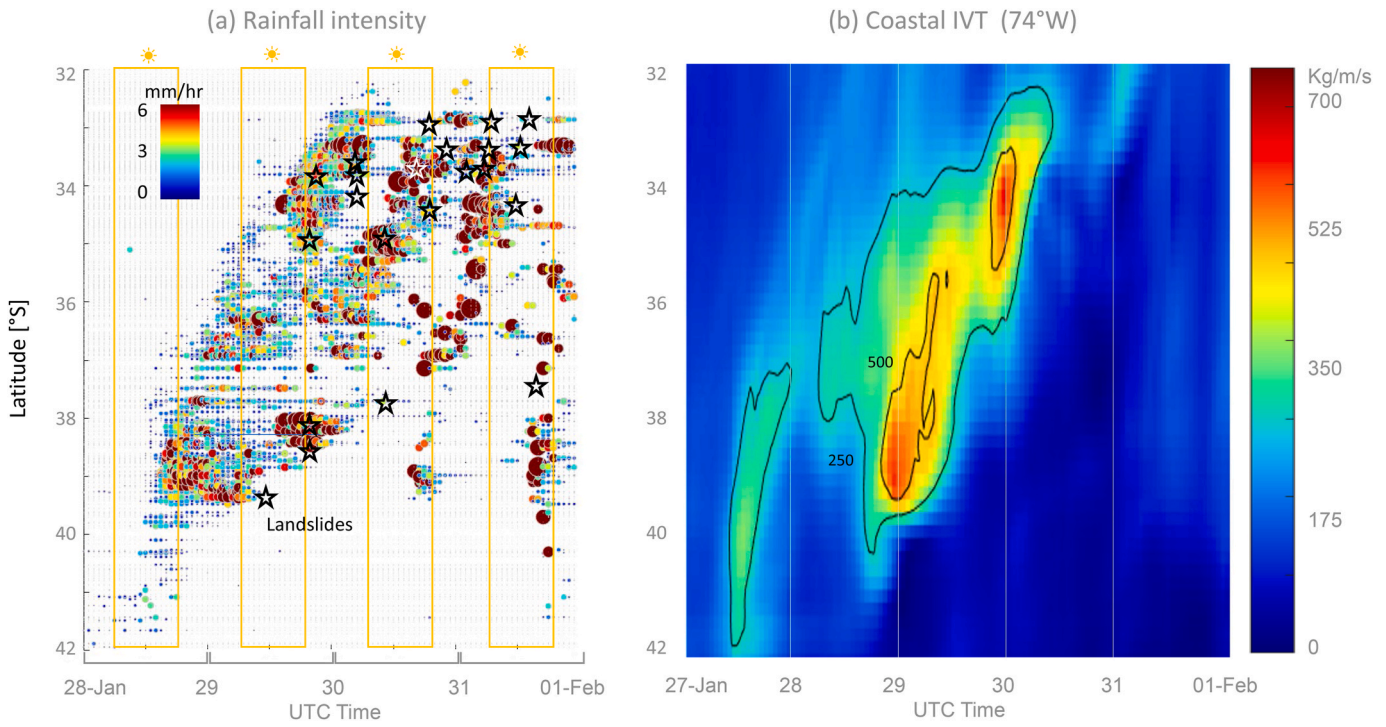

Fig. 3. (a) Time-latitude cross-section of *in-situ* hourly rain rates observations. The intensity in each station is plotted regardless of their longitude. Red stars in panel indicates landslide occurrence at a given time and latitude. (b) Time-latitude cross section of Integrated Water Vapor Transport (IVT, shaded in units of kg m^{-1} s^{-1}) along 74°W (approximately the Chilean coast). Black lines outline the 250 and 500 kg m^{-1} s^{-1} values. The dashed box indicates the domain cover in panel (a). Data source: ERA5. (For interpretation of the references to color in this figure legend, the reader is referred to the Web version of this article.)

triggered by anomalous convection over the warm pool region and SPCZ (e.g., Shimizu and de Albuquerque Cavalcanti, 2011; Rondanelli et al., 2019).

Of particular relevance for the subsequent storm development was the establishment of a tropospheric-deep anticyclone/ridge at high latitudes. A well-developed MJO -with amplitude near 2 according to the RMM index and between phases 6 and 7- was present during the ten days previous to the storm, consistent with the extratropical Rossby wave response originating the high latitude blocking high. A time-longitude Hovmöller diagram of the 500 hPa geopotential height anomalies at 60°S (Fig. 5b) reveals that the positive center (around 150°W) remained stationary from January 15 to 21 and then slowly drifted eastward (~5 m s^{-1}), reaching the far eastern Pacific by the end of January. Towards the end of this period a cyclone formed at low and mid-levels to the north of the blocking high (Fig. 5c). Southeasterly winds downstream of the blocking high advected cold air into lower latitudes while northwesterly winds downstream of the closed low advected moist and warm air from its subtropical reservoir into the southeast Pacific. The interplay of these two factors in the subsequent storm development is explored next.

3.4. Synoptic-scale environment

The synoptic evolution during 26–31 January 2021 is illustrated in Fig. 6 by maps every 24 h of the 500 hPa geopotential height (contours), precipitable water (colors) and 700 hPa wind speed (grey shading outlines wind maxima). At 12 UTC 26 January, the aforementioned deep ridge at midlatitudes and closed low farther north were well defined over the central south Pacific (Fig. 6a). By this time a tongue of moist air (PW > 40 mm) had made its way from lower latitudes into the central subtropical Pacific. Wind convergence downstream of the high/low couplet acted to enhance the meridional temperature gradient in the free troposphere at midlatitudes, most marked around 90°W (Sup. Fig. 4). As a result, a westerly wind jet developed in the next 24 h extending from the eastern Pacific toward the Chilean coast centered at 35–40°S. The core of the jet was at around 300 hPa but strong zonal flow also prevailed in the middle and lower troposphere, promoting the rapid eastward extension of a moist air filament (Fig. 6b). This Zonal Atmospheric River (ZAR) made landfall along the coast of Chile at about 39°S by the end of 28 January (Fig. 6c). At this time the ZAR was collocated with the jet axis and to the north of a weak baroclinic zone in the lower and middle troposphere at about 38°S (not shown). Weakly stable conditions during the ZAR passage fostered the strong ascent in the vicinity of the Andean foothills (Sup. Fig. 5) increasing the orographic precipitation enhancement (Falvey and Garreaud, 2007). Radiosonde data at Santo Domingo (coastal zone, 33°S) and AMDAR data near the Santiago (33.5°S) reveal that 0 °C isotherm height (H_0) was at ~3500 m ASL on 29 January and dropped to 3300 m ASL the next day, well above the typical H_0 in winter storms (~2300 m ASL; Mardones and Garreaud, 2020). Recall that the subtropical Andes reach more than 5500 m ASL so the warm conditions during this storm magnified the hydrological response (see section 3.6).

Further details on the ZAR evolution can be obtained from a time-latitude cross section of IVT along 74°S (Fig. 3b). The main axis of the ZAR moved northward along the Chilean coast from late 28 January until its demise around midday of 30 January, in close synchrony with the first pulse of precipitation. Coastal IVT values (250–750 kg m^{-1} s^{-1}) and their persistence (24–36 h) indicate a moderate ZAR (category 2 out of 5) in the scale proposed by Ralph et al. (2019), yet this ZAR produced an exceptional situation for summertime in this subtropical latitude (see section 3.5). The arrival of the ZAR to central Chile (33–35°S) is also evident by the ERA5 area-mean series of zonal IVT (very similar to total IVT in this case, Fig. 4c) that, along with the zonal flow at 700 hPa and PW, reaches a maximum by the end of 29 January, just before of the maximum area-mean precipitation.

By midday of 30 January, the ZAR reached its northernmost latitude (32°S) and begun to fade rapidly as per the decrease in IVT (Fig. 4c). Nevertheless, moisture remained high and only reached pre-storm

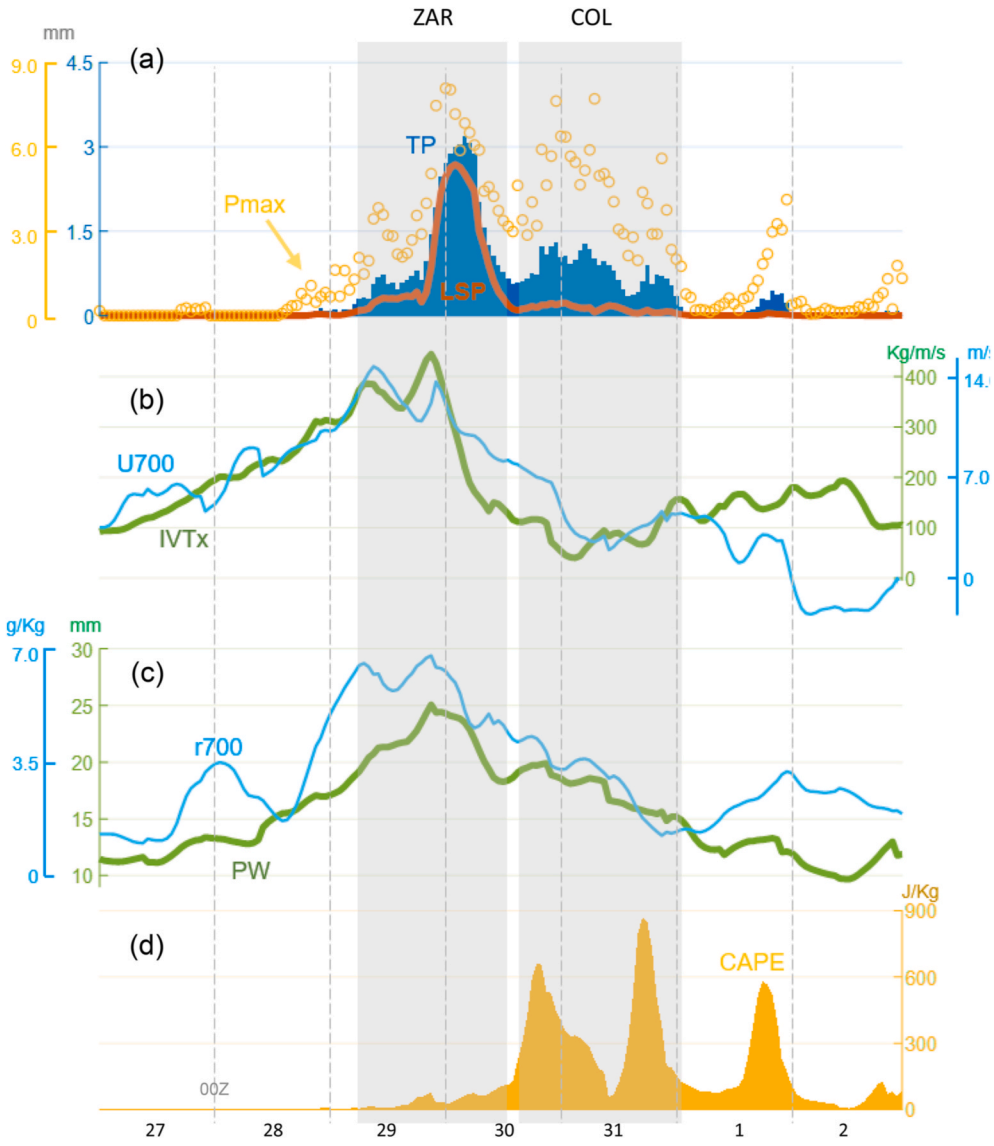

Fig. 4. Hourly time series of selected ERA5 variables in central Chile (average in the latitude-longitude box 33°–35°S and 69.9°W–72°W): (a) large scale (LSP, dark orange line), total precipitation (PT, blue bars) and maximum precipitation rate (light orange circles, note different scale), (b) zonal component at 700 hPa of wind (U700, light blue line) and zonal component of the integrated water vapor (IVTx, green line), (c) water vapor mixing ratio at 700 hPa (r700, light blue line) and column integrated precipitable water (PW, green line), and (d) convective available potential energy (CAPE, yellow area). The grey bands indicate the two stages of the storm: arrival of a zonal atmospheric river (ZAR) and development of a Cut-off low (COL) as identified in section 3d. (For interpretation of the references to color in this figure legend, the reader is referred to the Web version of this article.)

values 36 h later (Fig. 4b). At the same time, a trough began to develop along the coast of southern-central Chile (Fig. 6d). The development of cyclonic relative vorticity ($\xi < 0$) at mid-levels occurred rapidly during the last two days of the storm (Sup. Fig. 6) and was more evident between 700 and 500 hPa where a closed low centered 36°S, 75°W (just off the coast) formed during the morning of January 31. The depression at mid-levels was located well to the north of the polar jet so it can be described as a cut-off low (COL), although of short duration (<24 h) and with a limited expression in the upper troposphere. Such development was promoted by southerly winds downstream of the ridge over the south Pacific near the Chilean coast (Fig. 6e and f). Specifically, we verified that meridional advection of planetary vorticity was the leading element causing cyclonic development off central Chile in this part of the storm. Just to the north of the mid-level COL, strong NNW flow advected cyclonic vorticity toward the continent causing broader ascent over central Chile, somewhat stronger over the Andes foothill where topographic uplift was also present (Sup. Fig. 5). The mid-level southerlies off the Chilean coast also advected cold air, lowering H_0 to about 3100 m ASL on January 31 and February 1st, although these are yet elevated values compared to H_0 during winter storms. Moreover, the midlevel cooling contributed to the unstable thermodynamic conditions (i.e., CAPE>0) during the last two days of the storm.

Therefore, the synoptic conditions during the 28–31 January 2021 storm in the subtropical Andes had three distinctive phases. At least one week before the event, broad-scale circulation anomalies in the central south Pacific set the stage for the formation of long-lived zonal jet at midlatitudes that allows the development of a ZAR across the central-east south Pacific. In the second phase the ZAR reached the Chilean coast at about 39°S on 28 January and its axis moves northward to reach central Chile 24 h later. The ZAR provided the two ingredients for the first precipitation pulse: vast amounts of moisture (PW > 40 mm at the coast, 25 mm inland) and intense ascent right over the western side of the Andes of central-south Chile. During the third phase, the water vapour left by the ZAR served as a moisture source for the subsequent intense precipitation organized by the COL (e.g., Barahona, 2016). After the ZAR demise, the development of a short-lived, mid-level COL (centered near 36°S, 75°W) was promoted by a southerly flow and advection of planetary vorticity near the southern Chilean coast. North of the COL center, strong NNW flow caused cyclonic vorticity advection over central Chile. The ensuing broad-scale ascent acted in concert with unstable thermodynamic conditions to sustain scattered but intense convective precipitation that characterized the last half of the storm until the end of 31 January.

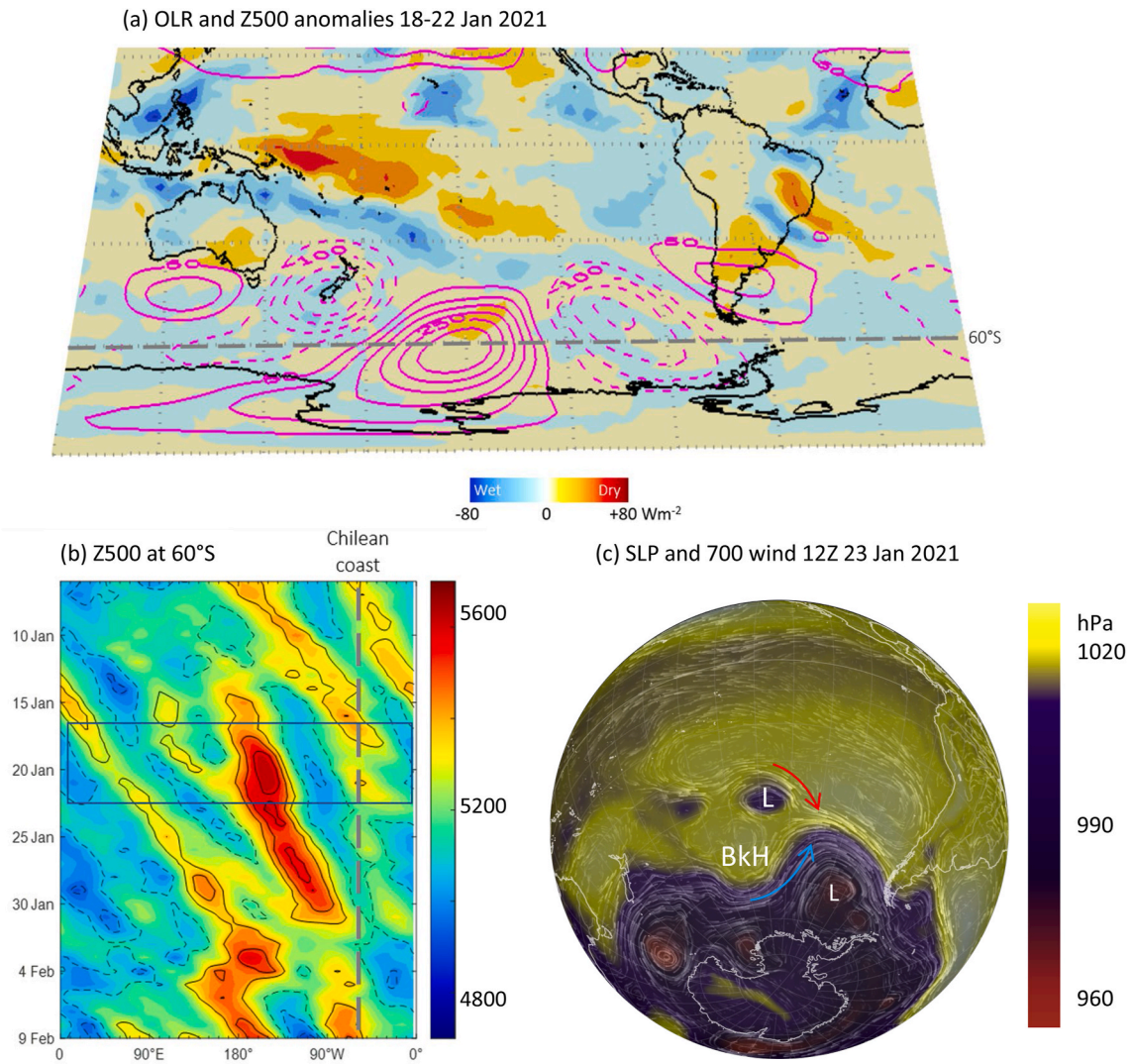

Fig. 5. (a) Outgoing longwave radiation (OLR, shaded) and anomalies of the 500 hPa geopotential height (contours every 50 mgp, positive in solid lines, negative in dashed lines) between 18 and 22 January of 2021. The anomalies are calculated as departures from the January long term mean. (b) Time-longitude of the 500 hPa geopotential height at 60°S from 5 January to February 5, 2021 (shaded). Also indicated are the anomalies every 100 mgp (solid lines positive anomalies, dashed lines negative anomalies). (c) Sea level pressure (shaded) and 700 hPa winds (vectors) at 12Z January 23, 2021. The red (blue) arrows highlight the warm/moist (cold/dry) advection downstream of the closed low (blocking high) at that time. Source: ERA5. (For interpretation of the references to color in this figure legend, the reader is referred to the Web version of this article.)

3.5. *Long-term perspective*

In this section we quantify the magnitude and uniqueness of the event by placing it on a long-time context. Fig. 7a shows the percentile of the daily maximum precipitation (P_x) in the period 28–31 January 2021. The distribution was calculated against the background of summer (DJF) daily data from 1961 to 2020 in a sample of stations with near complete records between 32 and 38°S. Along central Chile, P_x exceeded the 90th percentile and ranked among the five most rainy days (out of 5400) between La Serena (30°S) and Talca (35°S). In stations Quinta Normal – Santiago (33.5°S) and Talca (35°S), both located at elevations <1000 m ASL, the event brought the rainiest summer day since 1961. The same occurred in Lagunitas, located near Santiago but high in the Andes (~2800 m ASL). South of 35°S the event was copious but less extreme, although the precipitation recorded on 28 January in Temuco and Pucón exceeded the 95th percentile of the daily distribution. Furthermore, in all Chilean stations, the total accumulation during this event (Fig. 7b) exceeded the 95th percentile of the distribution and more than half experienced the largest 4-day accumulation on record. Along the same latitudinal range but over the Andes' leeside, the maximum daily precipitation recorded in January 2021 was not even among the 30 largest values. The storm total was also far from the highest historical rankings in that region.

These results show that the 28–31 January 2021 storm was extraordinary in the context of the precipitation in the last 60 years at low and high elevations in central Chile (32–36°S). The storm was also intense but not extreme farther south in Chile and over the lowlands in the lee of the Andes, consistent with the rainier summer conditions there (Aceituno et al., 2021; Mezher et al., 2012). A century long record in Quinta Normal (Santiago) provides further context where only 6 summer days (in six different years) had precipitation over 20 mm. Precipitation in two of these days was larger than the value recorded on January 29, 2021 (32 mm): February 4, 1945 (51 mm) and December 13, 1939 (38 mm). Similar results emerge when considering 2-, 3- and 4-day accumulations. Thus, although extraordinary, the 28–31 January 2021 storm in Santiago (and likely along central Chile) cannot be labeled as unprecedent in the historical context, with a recurrence period of ~33 years.

As discussed in section 3.2, the precipitation in central Chile during 29 January was mostly caused by the ZAR during first part of the storm

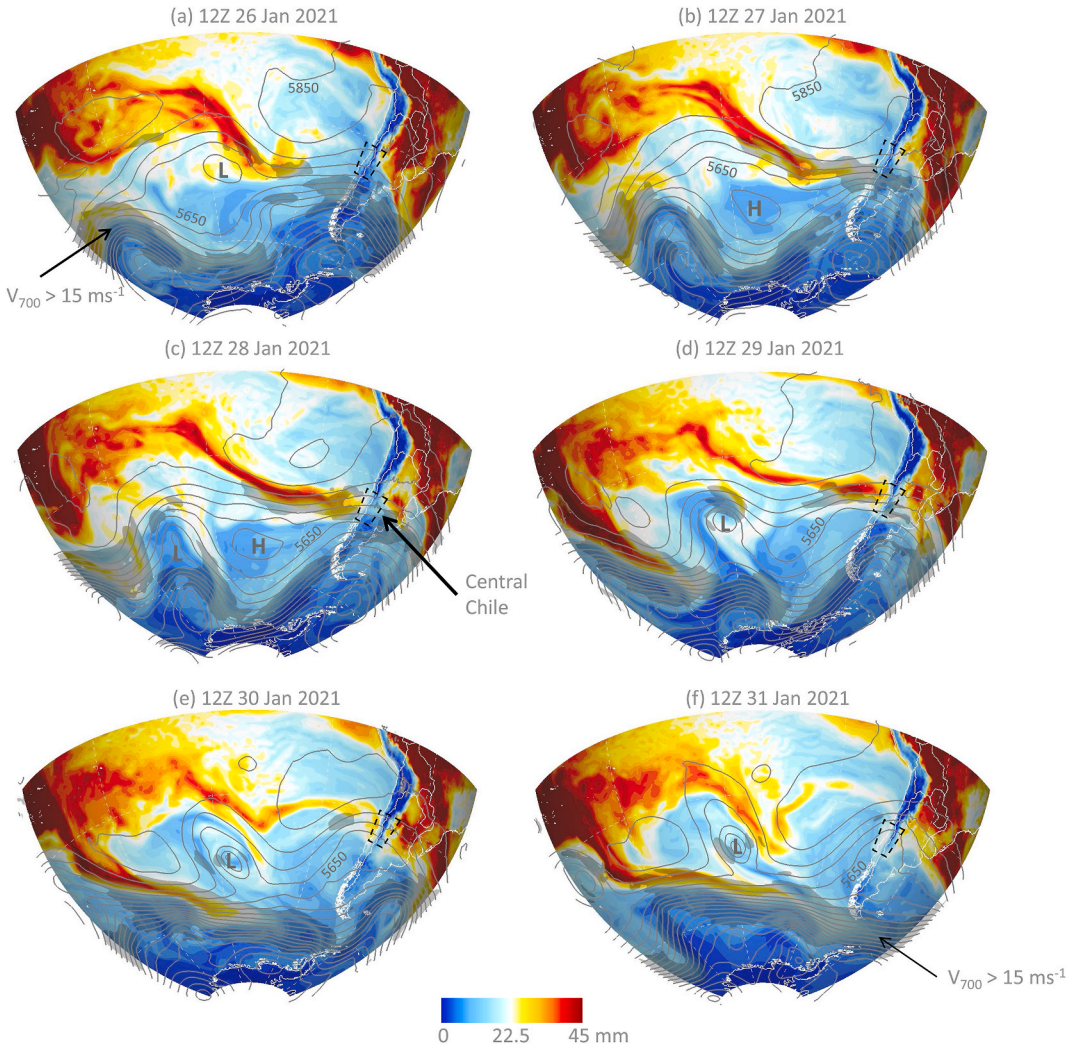

Fig. 6. Synoptic maps at 12Z from 26 to January 31, 2021. Each map includes 500 hPa geopotential height (contours, every 50 mgp), precipitable water (color shades, in mm) and 700 hPa wind speed (values exceeding 15 m/s are shaded in grey). The small, dashed box indicates central Chile. Data source: ERA5. (For interpretation of the references to color in this figure legend, the reader is referred to the Web version of this article.)

(historical extreme rainy days in Santiago seems also connected with ZAR; Sup. Fig. 7). The AR climatology of Viale et al. (2018) indicates that in average 1 or 2 AR make landfall between 33 and 34°S per summer, but it is based on the 85th percentiles of monthly IVT. Fig. 8a shows that the fixed 250 kg m^{-1} s^{-1} IVT value, widely used as baseline in other AR identification algorithms and in the AR scale of Ralph et al. (2019), has a very low probability of occurrence between 33° and 34°S (<1%) during summertime, as well as a value of 500 kg m^{-1} s^{-1} (the baseline to AR category 2) is virtually non-existent. Indeed, the 28–31 January ZAR is within the top 10 summertime AR storms since 1979 mainly at coastal grid points between 33° and 34°S, just surpassing the 250 kg m^{-1} s^{-1} IVT value (Fig. 8b).

In sum, part of the exceedingly large precipitation during 28–29 January 2021 can be explained by the warm, zonal character of this AR and its higher IVT (~300–500 kg m^{-1} s^{-1}) compared with more typical summer events (~150 kg m^{-1} s^{-1}, Viale et al., 2018). When considering the unusually high accumulation during the full event one should also recall that its second phase of convective in nature, made a significant contribution. Therefore, it was the combination of a strong ZAR and the subsequent COL that resulted in the large accumulation during the 28–31 January 2021 storm over central Chile, whose main impacts are discussed in the next section.

3.6. Impacts

Urban and rural flooding in Central Chile can be caused by storms with precipitation rates merely exceeding ~30 mm day^{-1} (e.g., Valenzuela and Garreaud, 2019). The hydrological impact of the storm is further amplified when precipitation occurs under warm conditions since high freezing levels augment the pluvial area of Andean basins where most rivers have their heads (e.g., Garreaud, 2013; Valenzuela and Garreaud, 2019). Consistent with its magnitude (60–100 mm) and warm nature (H_0 > 3000 m ASL), the 28–31 January 2021 storm produced significant impacts. The most damaging situation was the occurrence of 33 landslides reported and mapped by the Ministry of Public Works complemented with news reports. Overall, the short lived but intense rainfall period during the COL (final) stage of the storm caused almost twice as many landslides compared with the ZAR (initial) stage. Their temporal-latitudinal location is shown in Fig. 3a, revealing that most of the reported landslides occurred by the end of 30 and during 31 January between 33 and 35°S (Metropolitan and O'Higgins regions), although more events may have occurred unreported in other sparsely populated Andean sectors. Romero et al. (2022) also describe a catastrophic hail-debris flow in isolated mountains of the central valley. The sudden increase in river flow and numerous landslides, in turn, caused dozens of roadblocks including cuts in two international routes and dozens of tourists stranded in the mountains for 3 days. The Chilean

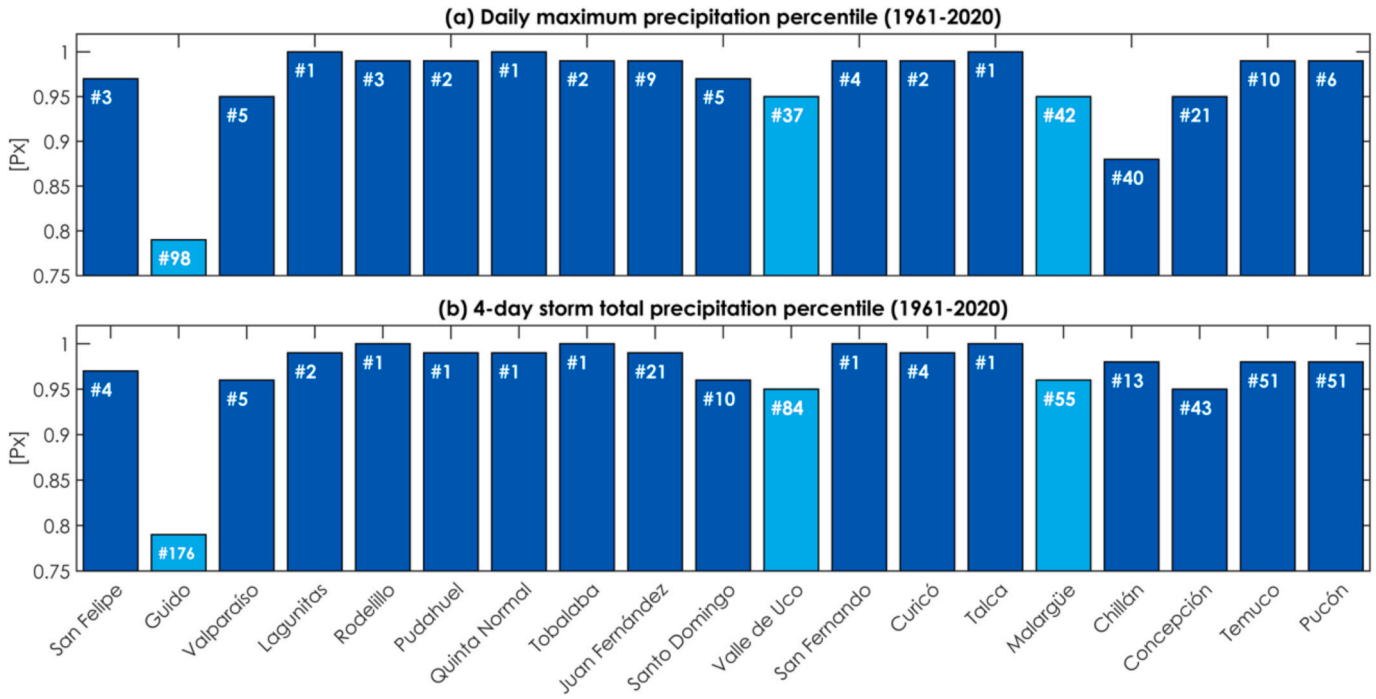

Fig. 7. (a) Percentile of the maximum daily precipitation between 28 and 31 January 2021 calculated from daily data between 1961 and 2021 for the summer season (DJF). (b) As in (a) but for the 4-days accumulated between 28 and 31 January 2021, calculated from all the 4-days moving accumulated data. Dark (light) blue bars represent gauges on the windward (leeward) of the Andes. Numbers on bars show the historical ranking considering the 1961–2021 period. Weather stations listed left to right represent north to south orientation. (For interpretation of the references to color in this figure legend, the reader is referred to the Web version of this article.)

Emergency Office also reported near 1000 people affected, 400 damaged houses and 170.000 homes without electricity for up to four days during the convective phase of the storm (ONEMI, 2021). Likewise, heavy precipitation and hail caused falling fruit trees, orchards and vineyards, resulting in widespread agricultural damages across central Chile at the top of the productive season (FEDEFRUTA, 2021).

The hydrological impacts of the storm are well captured by hourly records at station Maipo en El Manzano (location in Fig. 1a, data in Fig. 9). The station is located in the Andean foothills close to Santiago (33.6°S, 850 m ASL) and defines a basin of 4900 km^2 that was severely affected by landslides (Sup. Fig. 8). Although the Maipo river flow peaks in the middle of the summer (snow-melt regime), the dry conditions during the winter of 2020 resulted in a discharge of ~40 $m^3\ s^{-1}$ (one third of the long term mean values) weeks before the storm. The first (ZAR-phase) pulse of precipitation during 29 January caused an increase to 240 $m^3\ s^{-1}$ within 24 h and a rapid recess. The subsequent convective pulses (COL-phase) raised the flow to ~500 $m^3\ s^{-1}$ by the end of 31 January, followed by a recess to low pre-storm values by 2 February (Fig. 9a). A Ten-fold (or larger) increase in river flow was observed in many other Andean rivers along central Chile.

Measurement of the water turbidity (nephelometric turbidity unit, NTU) is an excellent proxy of the suspended sediment concentration reflecting the upstream erosive processes, such as earthquakes (Tolorza et al., 2019), snow and ice melt (Mao and Carrillo 2017) and rain-driven landslides (Vergara et al., 2022). Before the storm, turbidity was around 2.000 NTU -a high but common value in the Maipo river- raising to 20.000 NTU soon after the first pulse of precipitation and reaching nearly 60.000 NTU between 31 January and 1 February (Fig. 9b). These are extremely high values ranking within the top 10 records considering hourly time series from 1990 onwards, resulting in a suspended sediment load of about 10 ton s^{-1}. Noteworthy, the Maipo river is the main source of potable water for the more than 7 million inhabitants of Santiago, with an intake not far from El Manzano. The treatment plant suspends its operation when turbidity exceeds 4.000 NTU, a condition that prevailed for 64 h in connection with the 28–31 January 2021 storm (the 3rd longest period on record). Unlike previous events, the storm did not cause drinking water cuts thanks to the recently built mega-ponds of $1{,}5 \times 10^6$ m^3 that provide 34 h of drinking water supply autonomy.

Storm related impacts continued beyond the precipitation period. Crops were damaged by the appearance of fungi in the unusual warm and humid environment after the storm that added to the impact during the storm, produced losses of approximately US$ 600 million (FEDEFRUTA, 2021). The rain, however, caused a few weeks of greening in areas cover by sparse natural vegetation in central Chile during the otherwise bone-dry summer, clearly seen in the photosynthetic vigor estimates from satellites (Sup. Fig. 9). Despite the storm warm nature, snow blanketed the subtropical Andes above 4000 m ASL (Sup. Fig. 10). This unusual snowpack began to melt by February 3, 2021, when air temperature raised back to summer mean values (Fig. 9c), causing another 5 days during which turbidity exceed 4.000 NTU in the Maipo river (Fig. 9b). The post-storm rapid melting also seems the cause of a landslide on February 5, 2021 that blocked the Colorado river (tributary of the Maipo river) forcing evacuation of downstream towns because of the formation of a lake that reached 38.644 m^2 before it was drained a week later by emergency workers (Chilean Survey of Geology and Mining, 2021).

3.7. Forecasting of the 28–31 January 2021 storm

Despite its extraordinary nature, the storm did not cause deaths, which is surprising considering that in the affected area (7 Chilean regions and 2 Argentine provinces) there were 940 deaths between 1970 and 2014 due to extreme hydrometeorological events, considering floods, snow avalanches and landslides (DesInventar, 2021). This was probably due to the weather forecast and the effective evacuation of people at risk by the emergency authorities. Here we evaluate the performance of the QPF on the basis of the current generation of GFS. Knowing strengths and weaknesses of QPF products is key for

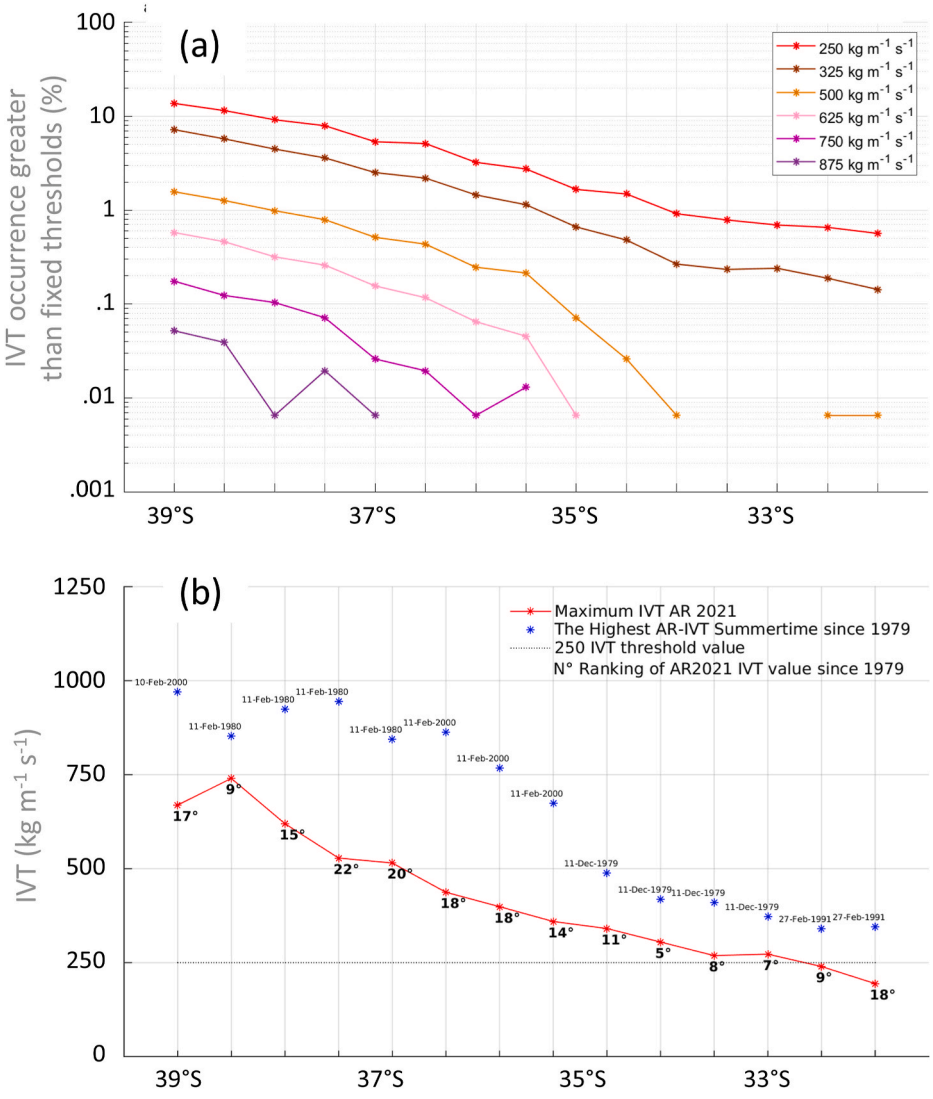

Fig. 8. (a) Percentage of occurrence of different IVT threshold values at grid points along the Chilean coast considering the summer season (DJF) 1979–2021 climatology based on the Climate Forecast System Reanalysis data (Saha and Co-authors, 2010). b) Maximum IVT values during the end of January 2021 AR storm and the highest IVT values during AR conditions, according to the AR-identification algorithm in Viale et al., (2018). The rank of the end of January 2021 AR storm among all summertime ARs since 1979 as a function of latitude is also indicated.

first-response authorities and meteorological service officers that use this information as input to make timely decisions.

GFS is currently run by the U.S. National Weather Service at 0.25° × 0.25° lat-lon, with four cycles per day and provides forecast up to 16 days in advance.[2] The model considers 127 vertical layers from surface up to ~80 km, including land-soil and sea-surface variables. Given its public availability, GFS outputs are widely used by research and operational communities worldwide as a guide for local forecast and boundary conditions for area limited models. For instance, the Chilean Weather Service (DMC) runs the Weather Research and Forecasting (WRF) model at 3 km resolution using GFS as boundary conditions.

We begin our analysis by considering the spatial distribution of accumulated precipitation (hereby called APCP) over the storm period (28–31 January 2021) using the forecasts initialized at 00 UTC of the previous 6 days (Fig. 10). The APCP can be contrasted with the observed accumulation presented in Fig. 2a and b. Six days before the storm (Fig. 10a) accumulations surpassing 100 mm were predicted to occur between 37°S and 40°S over the windward side of the Andes (over forecast), but less than 10 mm was predicted over central Chile (under forecast). The APCP pattern was similar in the forecast issued on January 23 (Fig. 10b). Four days before the storm the GFS began to predict significant precipitation (>20 mm) over the Andes of central Chile (Fig. 10c). Three days before the storm (Fig. 10d) GFS shows a maximum accumulation extending south of 40°S and decreasing in magnitude north of 36°S, maintaining the same indication with the highest impact along the Andes' windward side. Two days before the storm (Fig. 10e) the maximum accumulation south of 36°S decreases to less than 120 mm while a more extended area of ~120 mm is evident between 34°S and 36°S. Finally, one day before the storm (Fig. 10f), the QPF displays two areas with maximum accumulation of ~120 mm, one between 34°S and 35°S and the other between 36°S and 38°S, with the latter extending more towards the coast. Overall, the APCP pattern predicted by GFS runs initialized less than 48 h before the storm onset shows a distribution in good agreement with the observations. For instance, the spatial correlation between GFS runs (Fig. 10e and f) and observations (Fig. 2a) varies between $R^2 = 0.58$ and $R^2 = 0.68$ in this period. GFS, however, tends to over forecast accumulations over the entire domain, specially over the windward slope of the Andes, where predicted accumulations are up to 2 times larger than observed. Keep in mind, however, the poor observational basis over high terrain.

More details about the QPF performance of GFS using the observed gridded precipitation (Fig. 2a) are obtained using 4 traditional forecast verification metrics (Wilks, 2011; Wolff et al., 2014; see Appendix A for details) applied to the 96-h accumulations between 28 and 31 January

[2] https://www.emc.ncep.noaa.gov/emc/pages/numerical_forecast_systems/gfs.php.

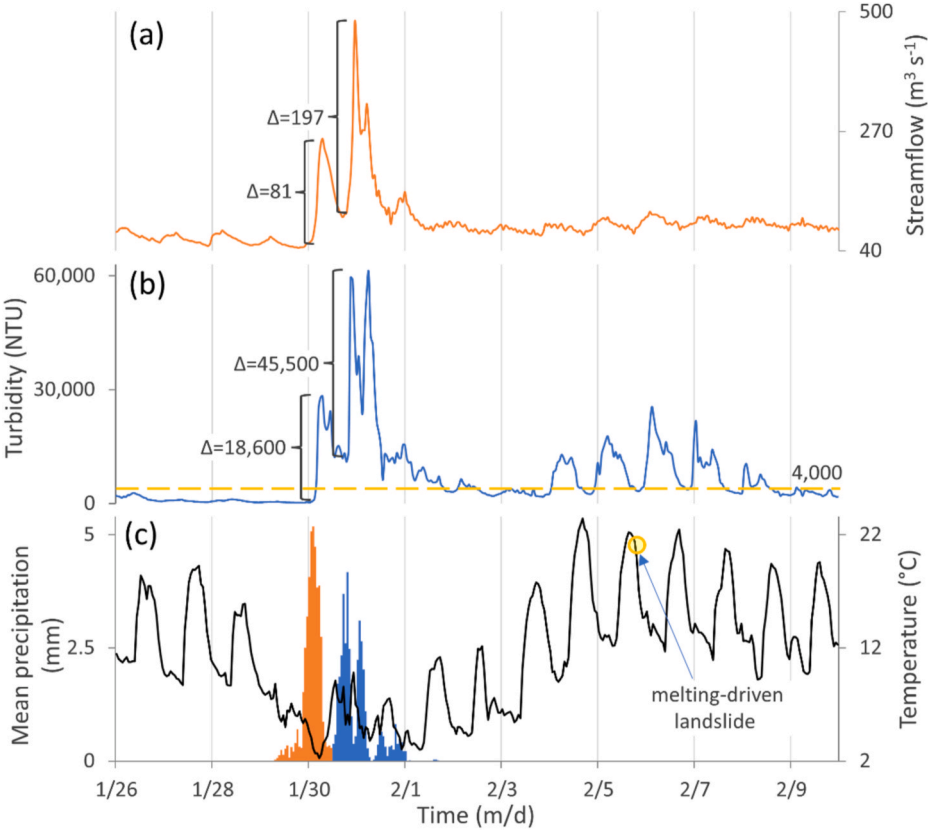

Fig. 9. Hourly series of (a) streamflow at Maipo en el Manzano (33.6°S, 70.2°W, 850 m ASL) and (b) turbidity at Maipo en la Compuertas (8 km downstream from El Manzano) during the end of January and early February 2021. (c) Precipitation averaged for seven rain gauges within the basin defined by Maipo en el Manzano and air temperature at the Embalse El Yeso station (2.5 km ASL, located in the basin centroid). Color coded precipitation in divides the period with ZAR and COL. (For interpretation of the references to color in this figure legend, the reader is referred to the Web version of this article.)

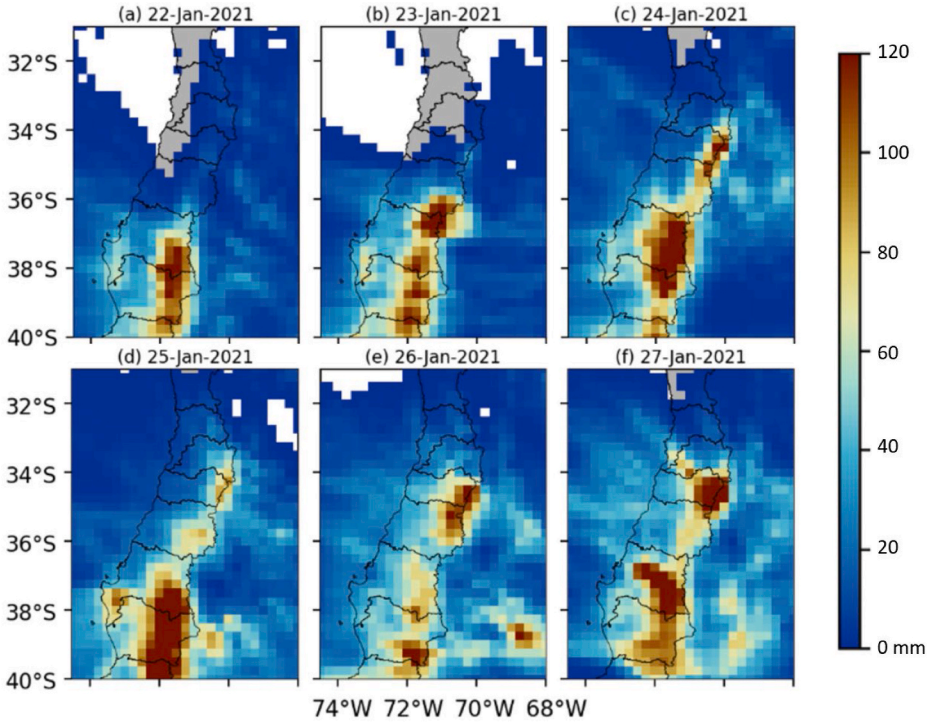

Fig. 10. Storm accumulated precipitation (APCP, 28–31 January 2021) from GFS-QPF. Different initial dates at 00 UTC are displayed, from (a) 22 January (lead hours 150 to 240) to (f) 27 January (lead hours 30 to 120).

2021: probability of detection (POD), false alarm ratio (FAR), frequency bias (FBIAS), and critical success index (CSI). All of them are based on a 2 × 2 contingency table that represents the joint probability of the occurrence and no-occurrence of an event versus forecasted and no-forecasted events (Murphy and Winkler, 1987). In this case, for a given initialization time, the frequency of events is defined by the

number of grid cells that reach an APCP thresholds of 96-h equal or larger than: 0.1, 0.5, 1, 5, 10, and 20 mm.

Fig. 11 displays the results for the abovementioned forecast verification metrics from 6 days (22 January) to 1 day (27 January) previous to the storm verification period (28–31 January). The metrics indicate a QPF performance that improves as the initialization time approaches the valid time, depicted by POD and CSI tending to 1 and FAR tending to 0 from 22 to 27 January (Fig. 11 a-c). Considering the APCP thresholds, GFS-QPF has a better performance for lower-valued accumulations, especially for runs initialized after 24 January. Unlike the other metrics, FBIAS shows relative low variation as a function of APCP thresholds (Fig. 11d). However, for different initial time FBIAS shows mixed results: under forecast (less events forecasted than observed) for days 22–23 January, unbiased forecast for day 24 January, over forecast (more events forecasted than observed) for days 25–26 January and nearly unbiased forecast for day 27 January.

Moving toward the local-scale we take a look at the performance of the 6-hr accumulations predicted by GFS over a single grid cell over San José de Guayacan in the upper Maipo River Basin, one of the most impacted locations during the storm. Observed precipitation there began around 00 UTC of January 30 and extended for the next 48 h as shown in the lowest row in Fig. 12. The upper rows show the 6-hr precipitation forecast issued at different initial times (from 10 days before the observed onset). GFS forecast began to predict significant precipitation (>5 mm h^{-1}) for this location by 12 UTC 23 January (initial time), about 7 days before the event (lead time). Subsequent initial times indicated 6-h accumulations exceeding 10 mm during the storm period that was correctly anticipated. There was, however, substantial variability in the storm behavior among GFS cycles. Even forecasts issued one day ahead of the storm misses the right evolution of the precipitation. They tended to over forecast the rainfall intensity during 30 January (caused by the ZAR and more stable phase) and under forecast the intensity during the next 36 h (caused by the COL and more convective phase).

Until now we have addressed the skill of the GFS control forecast but, nowadays, international operational centers further provide ensemble forecast that allow exploring prediction skill in a probabilistic way. A historical perspective of the methods and applications of ensemble forecasts and probabilistic predictions is provided by Kalnay (2019). Of particular interest, Cordeira et al. (2017) analyzes the skill of the NCEP Global Forecast System (GFS) and Global Ensemble Forecast System (GEFS) in predicting AR during the CalWater 2015 field campaign centered in California (USA), and Ramos et al. (2020) investigate the skill of the ECMWF Integrated Forecast System Ensemble (IFS-ENS) in predicting AR landfalling in the Iberian Peninsula during winter. Although a complete evaluation of ensemble forecasting for the late January 2021 event in Chile is beyond the scope of this paper, we briefly explore this issue by considering the GEFS predictions (section 2).

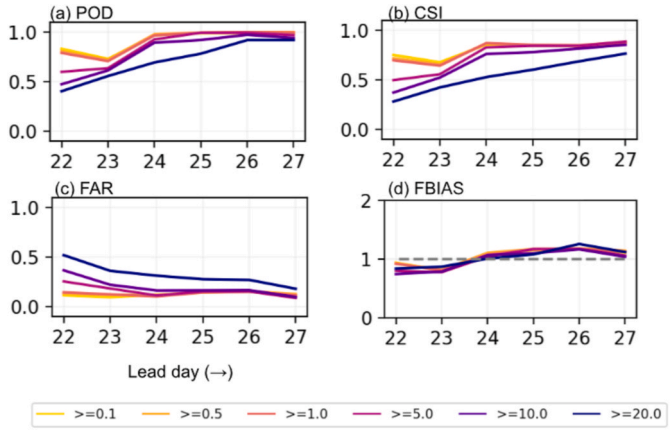

Fig. 11. Forecast verification metrics for GFS-QPF 96-h accumulation between 28 and 31 January and lead days 22 January (6 days in advance) to 27 January (1 day in advance). The verification metrics consider the observed gridded precipitation of Fig. 2a. Metrics include: (a) probability of detection (POD), (b) critical success index (CSI), (c) false alarm ratio (FAR), and (c) frequency bias. Color coded are different accumulated precipitation (APCP) thresholds. (For interpretation of the references to color in this figure legend, the reader is referred to the Web version of this article.)

Fig. 13 shows the 700 kg m^{-1} s^{-1} IVT contour for each of the GEFS members valid at 12 UTC January 29, 2021 (target time), when the ZAR was approaching the coast of central Chile. Each panel include the IVT forecast at different initial times superimposed on the observed contour. The ZAR (as visualized by the selected contour) over the far eastern Pacific was forecasted even 6 days ahead of the target time but with substantial spread in its position and an overall poleward bias of its actual location. As the initial time became closer to the target date the forecasted ZAR became more consistent and fits closer to the observed ZAR. It is notable how coherent were the GEFS members initialized 24 h before the target time, with most simulated ZARs correctly located around the observed ZAR. The overall improvement in the probabilistic ZAR prediction as the lead time shortens is consistent with Ramos et al. (2020) results. Nonetheless, the correct ZAR prediction is only partially translated in better quantitative precipitation forecast. Supplementary Fig. 11 shows GEFS members, members mean and control run for 6-h accumulated precipitation (APCP) forecasted at 00 UTC January 28, 2021 (initialization time). Both large-scale and convective components are displayed and the observed 6-h APCP are included for comparison. Storm wise, the QPF showed large uncertainty associated mainly to the large-scale precipitation, especially after 00 UTC 30 January. This is likely associated with a precipitation transitioning from an Atmospheric River to a cutoff-low forcing.

4. Discussion and conclusions

The storm that affected the subtropical Andes (32–39°S, Fig. 1a) between 28 and 31 January 2021 left more than 50 mm of rain across the lowlands of central-southern Chile and parts of western Argentina, and over 100 mm at higher elevations (Fig. 2a and b). These are substantial accumulations over this semiarid region, even in the context of wintertime, wet-season events (e.g., Valenzuela and Garreaud, 2019). The end of January storm, however, took place in the middle of the austral summer when rainfall is largely absent (Fig. 1b; Aceituno et al., 2021), thus reaching an extraordinary character. Both the maximum daily precipitation and accumulation during the storm ranked among the five largest values since 1961 in many stations along the Andes foothills between 32 and 36°S (Fig. 7). In Santiago, the 32 mm recorded on January 29, 2021 have only been surpassed twice in the last 120 summers. The storm was also copious but not extreme in Chile to the south of 36°S and the leeside of the subtropical Andes.

The end of January 2021 storm was also unusual because its overall structure and evolution. Occasional thunderstorms during austral summer deliver rain over the highest part of the subtropical Andes posing a significant threat as they can trigger landslides, flashfloods and extreme turbidity in the Andean rivers (Garreaud and Viale, 2014; Vergara et al., 2022). Summertime convective precipitation tends to be short lived (<12 h), scattered, warm (freezing level >4500 m ASL), feed by moisture from the Atlantic and forced by shortwave troughs or cut-off lows approaching the region (Viale and Garreaud, 2014). In contrast, precipitation in the January 2021 storm persisted for several days (Figs. 2c and 3a), affected a north-south swath of more than 700 km, fell from offshore to the high Andes, and lowered the freezing level to about 3000 m ASL.

These distinct precipitation features are more akin to winter events (Falvey and Garreaud, 2007; Viale and Nuñez, 2011) and reflect the leading driver of the event: a zonal atmospheric river (ZAR) just to the north of a weak baroclinic zone over the southeast Pacific (Fig. 6). The axis of the ZAR landfalled at about 39°S on 28 January and moved

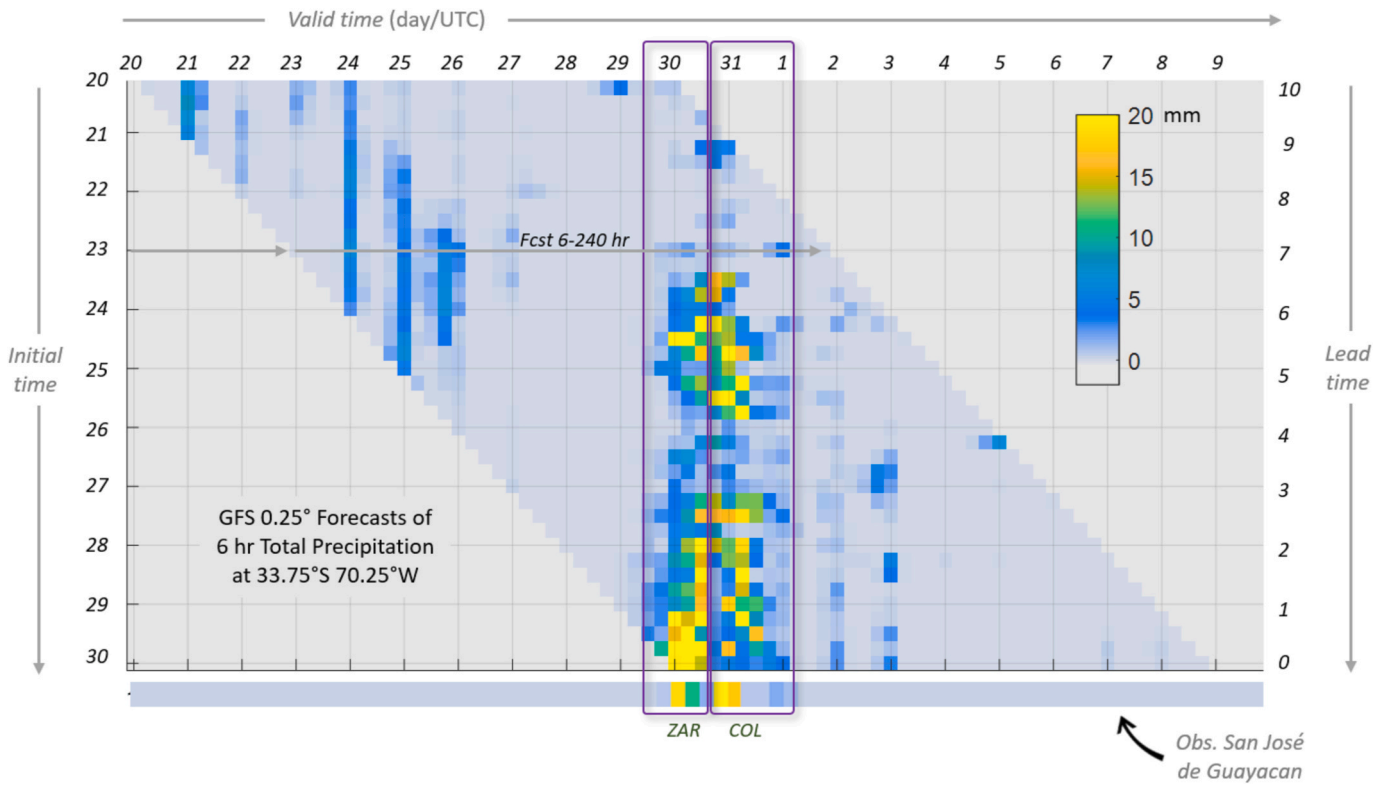

Fig. 12. Quantitative precipitation forecast (QPF) of 6-h accumulations at San José de Guayacan (33.7°S, 70.3°W, 1020 m ASL) from the Global Forecast System (GFS). Displayed are initial times between 06 UTC 20 January and 00 UTC 30 January, with 240-h of lead time. Last row shows observed 6-h accumulations at the same location. The purple rectangles indicate the approximate duration of the ZAR and COL phase of the storm. (For interpretation of the references to color in this figure legend, the reader is referred to the Web version of this article.)

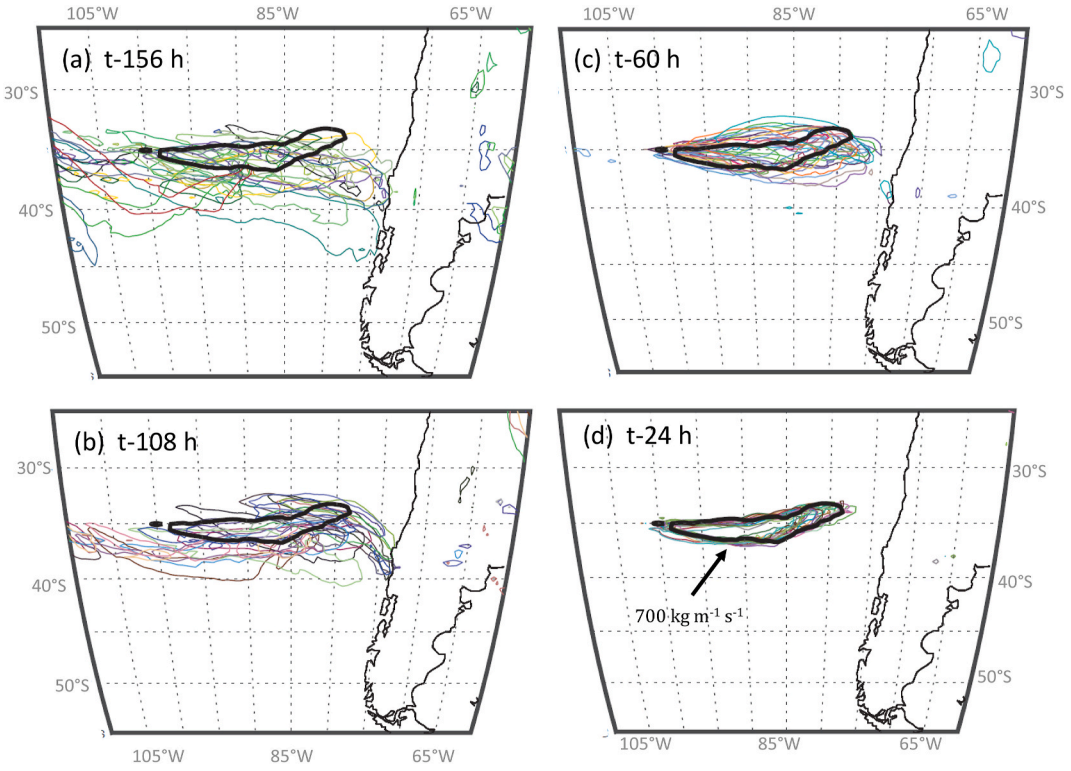

Fig. 13. Spaghetti diagram of 20 ensemble members of the GEFS V12 NCEP. The color contours show the 700 kg m^{-1} s^{-1} for each of the ensemble members. Initial times are indicated in hours before 12Z January 29, 2021 (target time). Black contour in each of the panels is the 700 kg m^{-1} s^{-1} contour from ERA5. (For interpretation of the references to color in this figure legend, the reader is referred to the Web version of this article.)

northward to reach 32°S two days later (Fig. 3b). Tropospheric deep, strong westerlies forced the ascent of moist laden air parcels over the windward side of the subtropical Andes resulting in widespread precipitation over central Chile, a marked orographic enhancement and spill over into lee side of the mountains. The moisture brought by the ZAR was also key for the subsequent convective precipitation promoted by a short lived cut off low (COL) at mid-levels. More broadly, atmospheric rivers have been identified as the causal factor behind flash floods and landslides, both in the winter and summer season, in many other mountainous regions, such as the Appalachian Mountains (Miller et al., 2019), northern and southern California (Cordeira et al., 2019; Oakley et al., 2018), east Asia (Kamee et al., 2017) and the Iberian Peninsula (Ramos et al., 2015).

Analogous to precipitation events, atmospheric rivers reaching central Chile are not uncommon in winter but hardly present to the north of 36°S during summer months (Viale et al., 2018) due to the strong and persistent subtropical anticyclone over the SE Pacific (Aceituno et al., 2021). This calls for large-scale circulation anomalies that we found were related to a blocking high over the South Pacific (Fig. 5), seemly in connection with anomalous tropical convection in the west side of the basin (Rondanelli et al., 2019). The blocking established by 18 January centered at 60°S 150°W and was accompanied by a low-pressure center at the same longitude but farther north. Poleward flow downstream of the depression transported moist, warm air from its tropical reservoir into midlatitudes, and equatorward flow downstream of the blocking high steepened the north-south temperature contrast over the eastern Pacific. These two ingredients, acting for more than a week prior to the central Chile storm, provided the conditions for the formation of the ZAR that rapidly moved eastward to reach South America (Fig. 6).

At the coast of central Chile, maximum IVT values reached ~500 kg $m^{-1}s^{-1}$ and persisted for more than 30 h (Fig. 3b), thus ranking the ZAR in category 2 (weak or moderate at the most) in the scale proposed by Ralph et al. (2019) to estimate the impact of atmospheric rivers. This relatively low category is at odds with the copious precipitation/high impact of this storm, but one needs to consider that the ZAR reached subtropical latitudes where IVT values tends to be lower than at midlatitudes (Fig. 8) (Viale et al., 2018). Furthermore, the tropospheric flow impinged the Andes nearly perpendicular and the ZAR took place in a warm environment ensuing liquid precipitation up to about 3300 m ASL. Indeed, warm storms can greatly amplify the hydrological response in Andean rivers (Garreaud, 2013; Mardones and Garreaud, 2020), calling for considering the elevation of the freezing level as an additional element to define an *ad-hoc* AR risk scale in regions of high topography.

Precipitation in central Chile (32–36°S) persisted for about 36 h after the passage of the ZAR (i.e., until the end of 31 January), a period during which the area mean rainfall subdued but when some of the highest intensities (>6 mm/h) were recorded (Figs. 3a and 4a). Downpours tended to occur simultaneous along the Andes foothills and higher terrain during evening and early night hours, accompanied by hail and lightning, indicative of a convective nature. At the same time, our synoptic analyses revealed the formation of cut-off low (COL) off the coast of central Chile in the wake of the ZAR (Fig. 6). The COL development was linked to negative planetary vorticity advection by wind blowing from south to north along the Chilean coast that also advected cold air at mid-levels. As seen in previous events (Garreaud and Fuenzalida, 2007) the COL fostered broad scale ascent over central Chile and unstable thermodynamic conditions (e.g., CAPE>0, Fig. 3d) that resulted in the final, convective stage of the January 2021 storm.

Most of the landslides and flashfloods were trigger by high rain rates/hail in the COL-convective part of the storm (Fig. 3a) when the soil was already saturated -because of the ZAR precipitation (Romero et al., 2022). Furthermore, the extremely dry conditions that have prevailed in central Chile for more than a decade (the so-called Central Chile Mega Drought: Garreaud et al., 2017, 2019) has been suggested as a preconditioning element for the landslide generation (Romero et al., 2022) In this sense, the end of January 2021 storm can be framed as an extreme compound event (e.g., Leonard et al., 2014). The soil failure and sudden increase in river flow (Fig. 9) caused dozens of roadblocks, dozens of tourists stranded in the mountains, near 1000 people affected, 400 damaged houses and 170.000 homes without electricity for up to four days. Heavy precipitation and hail also caused widespread agricultural damages. Despite its extraordinary nature, the storm did not cause deaths, probably due to the weather forecast and the effective evacuation of people at risk by the emergency authorities. In particular, GFS outputs began to forecast the event about 5 days before its occurrence. In that period, GFS provided a reasonable prediction of the timing and area affected by precipitation although it tended to over foreacast (under forecast) the magnitude at higher elevation during the ZAR (COL) phase of the storm (Figs. 10–12).

In closing this section, we note that this intense "winter storm" in the middle of the dry summer prompted questions on its connection with climate change. Although perceived as "unprecedent", the long observational record in Santiago reveals that the copious precipitation in late January 2021 was extraordinary but did occur a few times in the 20th century. No obvious trend is found in the occurrence of these rare events. While climate models consistently predict drier conditions for central Chile due to a decrease in winter precipitation (Boisier et al., 2019; Bozkurt et al., 2018), the fate of summer storms has not been addressed yet. A formal attribution study (contribution of climate change and natural variability) of the end of January 2021 storm is beyond the scope of this work but it is much deserved.

Author statement

Raúl Valenzuela: Writing original draft, Investigation, Methodology. **René Garreaud**: Conceptualization, Investigation, Writing original draft, Writing - Review & Editing. **Ivan Vergara:** Investigation, Formal analysis. **Diego Campos**: Investigation, Formal analysis. **Maximiliano Viale**: Investigation, Formal analysis. **Roberto Rondanelli**: Investigation, Formal analysis.

Funding

This work was supported by ANID, Chile, FONDAP/15110009. RG is partially funded by FONDECYT Regular grant 1211412. RR and RV are partially funded by ANID Anillo grant ACT 210046.

Declaration of competing interest

The authors declare that they have no known competing financial interests or personal relationships that could have appeared to influence the work reported in this paper.

Acknowledgments

We thank early discussion on the meteorological aspects of this event with Daniel Veloso, Luis Muñoz and Camilo Barahona. Natalia Silva (ONEMI) and Milo Millán (MOP) kindly shared technical information on the event' impact. Turbidity data of the Maipo river was kindly provided by Edson Landeros and Jorge Reyes from Aguas Andinas. We appreciate assistance from Camilo Menares and the staff at the Data Computing unit at (CR)2. Some in-situ rain measurements were supported by FONDECYT 11151009 and FONCYT 2016-1666 grants. Constructive comments by two anonymous reviewers help to improve the original manuscript.

Appendix B. Supplementary data

Supplementary data to this article can be found online at https://doi.org/10.1016/j.wace.2022.100472.

Appendix A

POD is the ratio between the number of events forecasted and observed and the total events observed and provides a metric of model discrimination (ability of the model to produce different outputs for different observed events). This metric has a positive orientation, with the best (worst) performance having a value of 1(0).

FAR is the ratio between events forecasted but not observed and the total events forecasted and provides a metric of model reliability. This metric has a negative orientation, with the best (worst) performance having a value of 0(1).

FBIAS is the ratio between total events forecasted and total events observed and provides a metric of model bias. The best performance is indicated by a value of 1 while worst performance show values »1 or approaching to zero.

Finally, CSI is the ratio between events forecasted and observed and the events that were either forecasted or observed and provides a metric of model accuracy. This metric has a positive orientation.

References

Aceituno, P., Boisier, J.P., Garreaud, R., Rondanelli, R., Rutllant, J.A., 2021. In: Fernández, B., Gironás, J. (Eds.), Climate and Weather in Chile. Water Resources of Chile, 8. Springer International Publishing, pp. 7–29 of World Water Resources.

Allen, M.R., Ingram, W.J., 2002. Constraints on future changes in climate and the hydrologic cycle. Nature 419, 228–232. https://doi.org/10.1038/nature01092.

Barahona, C., 2016. Precipitación asociada a bajas segregadas en el Hemisferio Sur. Universidad de Chile. https://repositorio.uchile.cl/handle/2250/140815.

Boisier, J.P., Alvarez-Garreton, C., Cordero, R., Damian, A., Gallardo, L., Garreaud, R., Lambert, F., Ramallo, C., Rojas, M., Rondanelli, R., 2019. Anthropogenic drying in central-southern Chile evidenced by long term observations and climate model simulations. Elem Sci Anth 6, 74. https://doi.org/10.1525/elementa.328.

Bozkurt, D., Rojas, M., Boisier, J.P., Valdivieso, J., 2018. Projected hydroclimate changes over Andean basins in central Chile from downscaled CMIP5 models under the low and high emission scenarios. Clim. Change 150, 131–147. https://doi.org/10.1007/s10584-018-2246-7.

Brown, B., Coauthors, 2021. The model evaluation Tools (MET): more than a decade of community-supported forecast verification. Bull. Am. Meteorol. Soc. 102, E782–E807. https://doi.org/10.1175/BAMS-D-19-0093.1.

Chilean Survey of Geology and Mining, 2021. Informe sobre condición de embancamiento en confluencia de Río Colorado con estero Las Vacas, comuna de San José de Maipo.

Cordeira, J., Ralph, M., Martin, A., Gaggini, N., Ryan, J., Neiman, P., Rutz, J., Pierce, R., 2017. Forecasting atmospheric rivers during CalWater 2015. Bull. Am. Meteorol. Soc. 98, 449–459. https://doi.org/10.1175/BAMS-D-15-00245.1.

Cordeira, J., Stock, J., Dettinger, M.D., Young, A., Kalansky, J., Ralph, M., 2019. A 142-year climatology of northern California landslides and atmospheric rivers. Bull. Am. Meteorol. Soc. 8, 1499–1509. https://doi.org/10.1175/BAMS-D-18-0158.1.

de Lima Nascimento, E., Ambrizzi, T., 2002. The influence of atmospheric blocking on the Rossby wave propagation in Southern Hemisphere winter flows. J. Meteorol. Soc. Jpn. Ser. II 80, 139–159.

DesInventar, 2021. Hydro-meteorological disasters of Chile. Retrieved from. https://www.desinventar.org/.

Dominguez, F., Coauthors, 2018. Tracking an atmospheric river in a warmer climate: from water vapor to economic impacts. Earth Syst. Dynam. 9, 249–266. https://doi.org/10.5194/esd-9-249-2018.

Donat, M.G., Lowry, A.L., Alexander, L.V., O'Gorman, P.A., Maher, N., 2016. More extreme precipitation in the world's dry and wet regions. Nat. Clim. Change 6, 508–513. https://doi.org/10.1038/nclimate2941.

Falvey, M., Garreaud, R., 2007. Wintertime precipitation episodes in Central Chile: associated meteorological conditions and orographic influences. J. Hydrometeorol. 8, 171–193. https://doi.org/10.1175/JHM562.1.

FEDEFRUTA, 2021. Se triplican perdidas de productores de fruta por catástrofe agrícola. Portal web de la Federación Nacional de Productores de Fruta consultado el 18 de febrero de 2021. http://fedefruta.cl/).

Garreaud, R., 2013. Warm winter storms in Central Chile. J. Hydrometeorol. 14, 1515–1534. https://doi.org/10.1175/JHM-D-12-0135.1.

Garreaud, R., Fuenzalida, H., 2007. The Influence of Andes on cutoff lows: a modeling study. Mon. Weather Rev. 135, 1596–1613.

Garreaud, R., Viale, M., 2014. Análisis de los fenómenos meteorológicos y climáticos que afectan la cuenca del río Maipo. Aquae Papers 5, 17–29.

Garreaud, R., Alvarez-Garreton, C., Barichivich, J., Boisier, J.P., Christie, D.A., Galleguillos, M., LeQuesne, C., McPhee, J., Zambrano-Bigiarini, M., 2017. The 2010-2015 mega drought in Central Chile: impacts on regional hydroclimate and vegetation. Hydrol. Earth Syst. Sci. 21, 1–21. https://doi.org/10.5194/hess-21-1-2017.

Garreaud, R., Boisier, J.P., Rondanelli, R., Montecinos, A., Sepúlveda, H., Veloso-águila, D., 2019. The Central Chile mega drought (2010-2018): a climate dynamics perspective. Int. J. Climatol. 1–19 https://doi.org/10.1002/joc.6219.

Garreaud, R., Vergara, I., Viale, M., 2021. ¿Una tormenta de invierno en pleno verano? Entendiendo el extraordinario evento de finales de enero de 2021 en Chile central. In: Centro de Ciencia del Clima y la Resiliencia (CR2). https://www.cr2.cl/analisis-una-tormenta-de-invierno-en-pleno-verano-entendiendo-el-extraordinario-evento-de-finales-de-enero-de-2021-en-chile-central-cr2/ (19 March 2021).

Guan, H., Zhu, Y., Sinsky, E., Fu, B., Zhou, X., Li, W., Xue, X., Hou, D., Cui, B., Peng, J., 2020. The NCEP GEFS-v12 reforecasts to support subseasonal and hydrometeorological applications. STI Climate Bull. 79–82. https://doi.org/10.25923/t4qa-ae63.

Hersbach, H., Coauthors, 2020. The ERA5 global reanalysis. Q. J. R. Meteorol. Soc. 146, 1999–2049. https://doi.org/10.1002/qj.3803.

Huffman, G.J., Bolvin, D.T., Braithwaite, D., Hsu, K., Joyce, R., Xie, P., Yoo, S.-H., 2015. NASA global precipitation measurement (GPM) integrated multi-satellite retrievals for GPM (IMERG). Algorithm Theoretical Basis Document (ATBD) Version 4, 26.

Kalnay, M.E., 2019. Historical perspective: earlier ensembles and forecasting forecast skill. Q. J. R. Meteorol. Soc. 145, 25–34. https://doi.org/10.1002/qj.3595.

Kamee, Y., Mei, W., Xie, S.P., 2017. Climatological relationship between warm season atmospheric rivers and heavy rainfall over East Asia. J. Meteorol. Soc. Jpn. 95, 411–431. https://doi.org/10.2151/jmsj.2017-027.

Leonard, M., Westra, S., Phatak, A., Lambert, M., van den Hurk, B., McInnes, K., Risbey, J., Schuster, S., Jakob, D., Stafford-Smith, M., 2014. A compound event framework for understanding extreme impacts. Wiley Interdisciplin. Rev.: Clim. Change 5, 113–128.

Mao, L., Carrillo, R., 2017. Temporal dynamics of suspended sediment transport in a glacierized Andean basin. Geomorphology 287, 116–125. https://doi.org/10.1016/j.geomorph.2016.02.003.

Mardones, P., Garreaud, R.D., 2020. Future changes in the free tropospheric freezing level and rain–snow limit: the case of Central Chile. Atmosphere 11, 1259. https://doi.org/10.3390/atmos11111259.

Meehl, G.A., Zwiers, F., Evans, J., Knutson, T., Mearns, L., Whetton, P., 2000. Trends in extreme weather and climate events: issues related to modeling extremes in projections of future climate change. Bull. Am. Meteorol. Soc. 81, 427–436. https://doi.org/10.1175/1520-0477(2000)081<0427:TIEWAC>2.3.CO;2.

Mendes, M.C.D., Trigo, R.M., Cavalcanti, I.F.A., DaCamara, C.C., 2008. Blocking episodes in the southern hemisphere: impact on the climate of adjacent continental areas. Pure Appl. Geophys. 165, 1941–1962. https://doi.org/10.1007/s00024-008-0409-4.

Mezher, R.N., Doyle, M., Barros, V., 2012. Climatology of hail in Argentina. Atmos. Res. 114–115, 70–82. https://doi.org/10.1016/j.atmosres.2012.05.020.

Miller, Douglas K., Miniat, Chelcy F., Wooten, Richard M., Barros, Ana P., 2019. An expanded investigation of atmospheric rivers in the southern appalachian mountains and their connection to landslides. Atmosphere 10. https://doi.org/10.3390/atmos10020071.

Modeling Center, Environmental, 2003. The GFS atmospheric model. Natl. Centers Environ. Predict. Office Note 442, 14.

Murphy, A., Winkler, R., 1987. A General Framework for Forecast Verification. https://doi.org/10.1175/1520-0493(1987)115<1330:AGFFFV>2.0.CO;2 pdf.

Neiman, P.J., Schick, L.J., Ralph, F.M., Hughes, M., Wick, G.A., 2011. Flooding in western Washington: the connection to atmospheric rivers. J. Hydrometeorol. 12, 1337–1358. https://doi.org/10.1175/2011JHM1358.1.

Nesbitt, S.W., Coauthors, 2021. A storm safari in subtropical South America: proyecto RELAMPAGO. Bull. Am. Meteorol. Soc. 102, E1621–E1644. https://doi.org/10.1175/BAMS-D-20-0029.1.

Oakley, N., Lancaster, J.T., Hatchett, B.J., Stock, J., Ralph, F.M., Roj, S., Lukashov, S., 2018. A 22-year climatology of cool season hourly precipitation thresholds conducive to shallow landslides in California. Earth Interact. 22, 1–35. https://doi.org/10.1175/EI-D-17-0029.1.

ONEMI, 2021. Informe de Emergencia: Monitoreo por Sistema Frontal entre Coquimbo y Los Lagos. Reporte No. 25 del 14 de febrero de 2021. Oficina Nacional de Emergencia. Ministerio del Interior y Seguridad Pública, Gobierno de Chile.

Pendergrass, A.G., Knutti, R., Lehner, F., Deser, C., Sanderson, B.M., 2017. Precipitation variability increases in a warmer climate. Sci. Rep. 7, 17966 https://doi.org/10.1038/s41598-017-17966-y.

Ralph, F.M., Rutz, J.J., Cordeira, J.M., Dettinger, M., Anderson, M., Reynolds, D., Schick, L.J., Smallcomb, C., 2019. A scale to characterize the strength and impacts of atmospheric rivers. Bull. Am. Meteorol. Soc. 100, 269–289. https://doi.org/10.1175/BAMS-D-18-0023.1.

Ramos, A., Trigo1, R., Liberato, M., Tomé, R., 2015. Daily precipitation extreme events in the Iberian Peninsula and its association with atmospheric rivers. Bull. Am. Meteorol. Soc. 16, 579–597. https://doi.org/10.1175/JHM-D-14-0103.1.

Ramos, A.M., Sousa, P.M., Dutra, E., Trigo, R.M., 2020. Predictive skill for atmospheric rivers in the western Iberian Peninsula. Nat. Hazards Earth Syst. Sci. 20, 877–888. https://doi.org/10.5194/nhess-20-877-2020.

Romero, J.E., Vergara-Pinto, F., Aguilar, G., Garcés, A., Montserrat, S., 2022. Triggering factors, behavior, and social impact of the January 2021 hail-debris flows at the Central Valley of Chile. Landslides. https://doi.org/10.1007/s10346-021-01830-2.

Rondanelli, R., Hatchett, B., Rutllant, J., Bozkurt, D., Garreaud, R., 2019. Strongest MJO on record triggers extreme Atacama rainfall andWarmth in Antarctica. Geophys. Res. Lett. 46 https://doi.org/10.1029/2018GL081475.

Rudlosky, S.D., Goodman, S.J., Virts, K.S., Bruning, E.C., 2019. Initial geostationary lightning mapper observations. Geophys. Res. Lett. 46, 1097–1104. https://doi.org/10.1029/2018GL081052.

Saha, S., Coauthors, 2010. The NCEP climate forecast system reanalysis. Bull. Am. Meteorol. Soc. 91, 1015–1058. https://doi.org/10.1175/2010BAMS3001.1.

Shimizu, M.H., de Albuquerque Cavalcanti, I.F., 2011. Variability patterns of Rossby wave source. Clim. Dynam. 37, 441–454. https://doi.org/10.1007/s00382-010-0841-z.

Tolorza, V., Mohr, C.H., Carretier, S., Serey, A., Sepúlveda, S.A., Tapia, J., Pinto, L., 2019. Suspended sediments in Chilean rivers reveal low postseismic erosion after the Maule earthquake (Mw 8.8) during a severe drought. J. Geophys. Res. Earth Surf. 124, 1378–1397. https://doi.org/10.1029/2018JF004766.

Valenzuela, R.A., Garreaud, R.D., 2019. Extreme daily rainfall in central-southern Chile and its relationship with low-level horizontal water vapor fluxes. J. Hydrometeorol. 20, 1829–1850. https://doi.org/10.1175/JHM-D-19-0036.1.

Vergara, I., Garreaud, R., Moreiras, S., Araneo, D., Beigt, D., 2022. Exploring landslides–fluvial suspended sediment association in a semi-arid basin in central Chile. Geomorphology 402, 1–7. https://doi.org/10.1016/j.geomorph.2022.108129.

Vergara, I., Moreiras, S.M., Araneo, D., Garreaud, R., 2020. Geo-climatic hazards in the eastern subtropical Andes: Distribution, climate drivers and trends. Nat. Hazards Earth Syst. Sci. 20 (5), 1353–1367. https://doi.org/10.5194/nhess-20-1353-2020.

Viale, M., Garreaud, R., 2014. Summer precipitation events over the western slope of the subtropical Andes. Mon. Weather Rev. 142, 1074–1092. https://doi.org/10.1175/MWR-D-13-00259.1.

Viale, M., Garreaud, R., Valenzuela, R., Garreaud, R.D., Ralph, F.M., 2018. Impacts of atmospheric rivers on precipitation in southern south America. J. Hydrometeorol. 19, 1671–1687. https://doi.org/10.1175/JHM-D-18-0006.1.

Viale, M., Nuñez, M., 2011. Climatology of winter orographic precipitation over the subtropical central Andes and associated synoptic and regional characteristic. J. Hydrometeorol. 12, 481–507. https://doi.org/10.1175/2010JHM1284.1.

Wilks, D.S., 2011. Statistical Methods in the Atmospheric Sciences. Elsevier.

Wolff, J.K., Harrold, M., Fowler, T., Gotway, J.H., Nance, L., Brown, B.G., 2014. Beyond the basics: evaluating model-based precipitation forecasts using traditional, spatial, and object-based methods. Weather Forecast. 29, 1451–1472. https://doi.org/10.1175/WAF-D-13-00135.1.

Zhang, P., Chen, G., Ma, W., Ming, Y., Wu, Z., 2021. Robust atmospheric river response to global warming in idealized and comprehensive climate models. J. Clim. 1–52. https://doi.org/10.1175/JCLI-D-20-1005.1.